

Gasimov, Peyruz, Volumetric velocimetry in the presence of refractive interfaces. Design and validation, M.S., Department of Petroleum Engineering, May, 2019.

In this report, we address the problem of visual metrology through refractive interfaces. In particular, we discuss the design and optimization aspects of velocimetry systems and describe our particle-tracking setup capable of providing volumetric velocity data. Velocimetry has become a stock tool in experimental fluid dynamics with applications ranging widely in disciplines and scales. The system developed here offers a large Field of View which is an essential improvement for characterization of transport in heterogeneous media. The design is tailored for studies in small-depth domains, such as replicas of fractures, however, the suggested engineering solutions may be used at more general settings. We present preliminary validation results resolving the velocity within an $800\mu m$ -thick Hele-Shaw cell. Additionally, we discuss in detail the manufacturing process of the plastic replicas used in the study.



VOLUMETRIC VELOCIMETRY IN THE PRESENCE OF REFRACTIVE INTERFACES. DESIGN AND VALIDATION

by

Peyruz Gasimov, B.S. Petroleum Engineering

A Plan B report submitted to the
Department of Petroleum Engineering
and the
University of Wyoming
in partial fulfillment of the requirements
for the degree of

**MASTER OF SCIENCE
in
PETROLEUM ENGINEERING**

Laramie, Wyoming
May 2019

Copyright © 2019

by

Peyruz Gasimov

Contents

1	Introduction	1
1.1	Motivation	2
1.2	Basics of particle-based velocimetry	4
1.3	Review of volumetric velocimetry techniques	10
1.4	Velocimetry in the presence of refractive interfaces	18
2	Hardware setup	23
2.1	Microfluidic chips	26
2.2	System aligning and focusing	28
3	Calibration	29
3.1	Review of camera models	30
3.2	Calibration protocol	32
3.3	Empirical model	34
3.4	Mechanistic model	35
3.5	Empirical calibration algorithm	40
3.6	Mechanistic calibration algorithm	41
3.7	Post-calibration protocol	44
3.8	Self-calibration	49
4	Experimental procedure	51
5	Data processing	52

5.1	Particle center localization	53
5.2	Cross-camera particle matching	53
5.3	3D reconstruction of particle positions	56
5.4	Cross-frame particle matching	57
5.5	Vector calculation and validation	59
6	Results	60
6.1	Calibration results	60
6.2	Experimental results	61
6.3	Error analysis	63
7	Summary	65
8	Practical notes	66
9	Recommendations	67

Acknowledgements

I would like to thank my scientific advisor, Prof. Mohammad Piri for his continued support of the work, as well as the members of my graduate committee: Prof. Khaled Gasem and Prof. Frederico Furtado. Also, I would like thank my family, friends, and colleagues at Piri Research Group for their endless support.

Peyruz Gasimov

University of Wyoming

May 2019

1 Introduction

In recent decades, velocimetry has seen an unprecedented amount of development and growth in the number of applications. A large collection of techniques varying in scale and underlying physics have been developed, such as Laser-Doppler Velocimetry (LDV), Hot-Wire Anemometry (HWA) and Molecular-Tagging Velocimetry (MTV). In this report, we are going to focus our attention on a certain class of velocimetry comprising multi-point, particle-based velocimetry methods. The idea of particle-based velocimetry is extremely simple and intuitive and can be illustrated with the following example. If we are posed with a challenge of eyeballing the direction and speed of wind while looking outside a window, we will most likely search for visual clues, such as swaying trees. The problem is immediately alleviated if it is also snowing outside. In fact, then, by observing the movement of the snowflakes, we can estimate the wind velocity vector potentially at any point of the visible space. This idea has been taken as the basis in the today widely-used Particle Image Velocimetry (PIV) and Particle Tracking Velocimetry (PTV). To measure velocity, we place particles in the moving fluid and register their motion later precisely calculating the fluid velocity field. As mentioned, PIV and PTV are multi-point measurement techniques, which is to say that the measurement is performed simultaneously (or almost so) in all the points of the measurement domain. This is contrasted to the single-point techniques, such as classical LDV and HWA. Particle-based

methods are non-intrusive since no device is submerged in the fluid potentially perturbing the flow. A correctly designed experiment will produce valid velocity data while minimizing the effect of the particles on the flow. In this report, we review the basics of particle-based velocimetry, explore a variety of volumetric velocimetry techniques, look at the challenges and offered solutions. Close attention is paid to the common problem of image-based metrology through refractive interfaces. We describe our 3DPTV setup and the engineering solutions offered therein. Finally, we present the preliminary validation results.

1.1 Motivation

Velocimetry has been extensively used to validate fluid dynamics models and discover new flow physics in both laminar and turbulent settings. Being an indispensable part of wind tunnel testing, velocimetry is used to optimize automotive [1], [2], aircraft [3] and building design [4]. In biomedical fields, we study flow in blood vessels and air flow in breathe ways [5]. Troutman et al. [6] have looked at biogenic vortical flows. Martin et al. [7] used PIV to study the fluid dynamics of human swimming. Velocimetry has helped to improve fuel cell efficiency [8] as well as investigate mixing in reaction beds [9]. Finally, a large body of velocimetry-enabled research has been conducted in the area of multiphase flow [10], [11], [12], [13] .

As can be seen, the majority of applications of velocimetry deal with liquid flows. This usually means that at least one phase boundary is present in

the experiments. For visual metrology this poses a problem since light rays penetrating the interface in a direction different from normal will change angle and lose some of their power. A similar problem appears not only in velocimetry applied to liquid flows but, generally, in imaging through refractive interfaces. The engineering solutions offered in this report, therefore, are applicable beyond the problem at focus. Similar problems, for example, can arise in underwater imaging by ROVs or airborne imaging of underwater structures [14], [15].

Of particular utility are velocimetry methods capable of providing 3D information on velocity. In the past few decades, a large number of such techniques have been conceived. These techniques will be reviewed in the subsection 1.3.

Our focus application is the measurement of transport in plastic replicas of natural fractures. Flow in fractures can be encountered in a variety of settings such as oil and gas extraction [16], aquifer remediation and CO_2 sequestration [17]. An estimated more than 20% of oil reserves are residing in fractured rocks [18]. Recently, the so-called fracturing boom in the oil industry has further amplified the need for understanding transport in fractures.

In this report, we describe the effort of designing and optimizing a 3D velocimetry setup tailored for studies of transport in single-fracture replicas. Besides the presence of refractive interfaces, another major challenge is the need for large Field of View (FOV) in transport experiments, since we are

typically interested in a long evolution of solute plumes [19], something typical micron-scale setups cannot deliver. In a similar work dedicated to shallow domains, Fuchs et al. [20] present results for only a $20\text{mm} \times 20\text{mm}$ region. Here, we are posed with a challenge of preserving micron resolution while augmenting the FOV.

Our setup is also capable of Laser-Induced Fluorescence measurements, however no demonstration of this is offered in this report.

Finally, we discuss the manufacturing of the plastic chips used in this study.

1.2 Basics of particle-based velocimetry

While a large variety of methods have been developed hitherto, in what follows, we are going to focus solely on two particle-based techniques: Particle Tracking Velocimetry (PTV) and Particle Image Velocimetry (PIV). Visual access to the flow domain is usually required, however, approaches like Endoscopic [21], Ultrasonic PIV [22] and X-ray PTV [23] circumvent this necessity.

The simplest PIV/PTV setup for single-phase, two-dimensional velocity measurements consists of a camera, a light source, aimed at the domain of interest, tracer particles and a processing unit. The flow domain is seeded with the tracers scattering the light coming from the source which, in turn, is captured by the camera. A minimum of two images, separated by a time interval Δt are required to reconstruct the velocity field using the processing algorithms briefly discussed below. Pulse lasers equipped with a Q-switch are

commonly used because of the beam-shaping flexibility, power and stability they can offer. Other sources providing polychromatic and/or continuous light, such as Xenon lamps and LEDs, are also commonly used [24], [25], [26], [27]. Typically, a Synchronizer orchestrates the joint operation of the camera and the laser.

Light scattering physics for particles larger than the wavelength of the incident light obeys the Mie solution of the Maxwell equations [28]. For smaller particles, Rayleigh approximation can be used, and, importantly, in that range, the scattering intensity drops rapidly with the decreasing particle size which may result in an overly low Signal-to-Noise ratio (SNR). This problem can be solved by using fluorescent tracers at the smaller scales. The fluorescent particles emit light in response to external stimulation, such as laser radiation. Each tracer species has got an associated excitation and emission spectra. Typically, an emission spectrum resides at longer wavelengths with the so-called Stokes shift separating the two peaks. Design of fluorescence-based velocimetry setup comprises, among other things, choosing the right combination of laser, tracers and optical filters. While the optimal choice of the components can be narrowed down by prior analysis and the use of tools such as Fluorescence SpectraViewer by Thermo Fischer Scientific [29] or other utilities alike, the final decision will most likely involve some trial and error, since the characteristic spectra of the particles are influenced by the properties of the hosting liquid [30].

In selecting the tracers, the developer also has to consider the motion

mechanics of the tracer particles. In that regard, the most important quality for the tracers is the ability to closely follow the flow. During low Reynolds number experiments, a particle is subject to the deterministic forces of gravity and drag and random perturbations resulting from Brownian motion of the surrounding molecules. The net effect of the deterministic forces is typically quantified by the Stokes number:

$$S_t = \frac{\tau_r}{\tau_s}$$

where τ_s is a characteristic timescale of the flow and τ_r is the response time of the particle to the velocity change calculated as [31]:

$$\tau_r = \frac{d_p^2 \rho_p}{18\mu}$$

At higher Reynolds numbers the Stokes law does not apply and the effects, such as inertial focusing [32] and Saffman lift force [33], [34] dominate particle dynamics. A more rigorous Basset equation then needs to be employed with necessary augmentations to account for additional external forces [35], [36].

At smaller scales, Brownian motion becomes a significant factor as the radius and mass of the particles get smaller. The error resulting from Brownian motion has been given by Santiago et al. [37]:

$$\epsilon_b = \frac{1}{|\mathbf{v}|} \sqrt{\frac{2D}{\Delta t}}$$

where \mathbf{v} is the mean flow velocity, D – molecular diffusion coefficient and Δt

is the time interval between frames.

Stokes' law can be used to model the gravity effect on the tracers [38]. To minimize gravity-induced errors, the density of the tracers needs to match the one of the fluid as closely as possible, which may be challenging for gas flow studies. For liquid flows, polymers such as polystyrene ($\rho \approx 1.05 \text{ g/cc}$) have found a wide application [31].

In summary, the selection process of a correct tracer particle size is a trade-off between SNR and the ability to follow the flow.

While there is little difference in the hardware setup and the data acquisition procedures of PIV and PTV, the two techniques have different data processing approaches. As mentioned above, a minimum of two images separated by a controlled time interval are necessary to calculate the velocity field. The PIV algorithm is based on cross-correlation technique. First, the frames are divided into a grid of partially-overlapping subregions, called Interrogation Windows, which determine the groups of neighboring particles. In the classical approach, all particles within the group are assumed to travel at nearly same velocity. Each subregion of the first frame is then cross-correlated with its neighborhood in the second frame. The resultant cross-correlation peak location is chosen as the most likely displacement for the particle group. The calculation can be performed in spatial domain, or, more efficiently, in the Fourier space taking advantage of FFT algorithms and the convolution theorem. More details on the PIV processing algorithm can be found in [39], [38].

Contrary to PIV, PTV tracks individual particles allowing to study the flow from a Lagrangian perspective, as the particles can be tracked through multiple frames. Lower seeding densities are required for PTV (especially for the 3-dimensional measurements) [25], [40]. The two basic steps of 2DPTV data processing include localization of particle centers in both images followed by cross-frame particle matching (tracking) wherein a match to a particle in the first frame is found in the second one. The displacement vector is then calculated as the difference of the positions of the particle and its match. To reduce particle matching ambiguity and obtain Lagrangian information, multi-frame tracking is often employed, i.e. the measured velocity in the previous frame pair is used to make an initial estimate of the particle position in the next frame and so on [41], [40]. In many applications, PIV is used to generate an initial guess for the PTV estimate. Alternatively, Xiong et al. [42] and Tokumaru et al. [43] use equations of motion to obtain the estimate. Such auxiliary methods yield more robust tracking algorithms which allow for higher seeding densities. Each of the PTV processing steps has seen a large number of suggested algorithms. Some of them are briefly reviewed in section 5.

The advantages of PIV lie in that since the motion of groups of particles is tracked, random noise such as the one arising due to diffusion effects is averaged out. Similarly, for steady-state flows, ensemble averaging of the correlation peak leads to improved validity of the measurements. On the other hand, spatial resolution of classical PIV suffers due to a relatively large size of

the Interrogation Windows. This may lead to problems resolving fine structures of flow [44], as well as introduce bias due to spatial averaging [45], [46]. This makes PTV a preferred choice in studies of near-wall flow, flow near phase boundaries, and generally, flows with high gradients. A vast amount of work has been done to improve that aspect of PIV. Techniques aimed at enhancing spatial resolution of PIV include Image deformation [47], Recursive Grid Refining [48] and Super-Resolution PIV [49], [50], [51] which uses standard PIV to generate an initial estimate for subsequent PTV processing. The finite thickness of the interrogation volume contributing to the correlation peak known as Depth-Of-Correlation, is another known limitation of PIV especially pronounced at micron scales [46] where the entire volume illuminated. For PTV, tracer size sets theoretical upper bound for spatial resolution, as flow features smaller in size than tracers, in principle, cannot be discerned. At this point, it is important to note that PTV tends to be more sensitive to SNR and, therefore, typically requires larger particles [24]. The velocity vectors obtained from PTV are tied to particle positions which are known with subpixel accuracy, as opposed to vectors assigned to the IWs during PIV processing. Due to lower seeding densities of PTV, one of the problems commonly reported [52], [53], [24] are data gaps in the measured unstructured velocity data. Several articles address this issue, using advanced interpolation schemes [54], [55], [56] and enabling calculation of gradient and vorticity from the unstructured velocity fields.

While PIV can offer ensemble averaging to take advantage of steady-state

flows, all things being equal, PTV can also significantly benefit from continued data acquisition [44], [57], since this makes possible using low seeding density which yields more reliable measurements. A high density of vectors can add further benefit through subsequent Vector Validation discussed in section 5.5. It has been noted that for the same number of vectors, PTV requires far less particles [58]. Lower seeding density can offer some benefits from the practical standpoint, as this would lead to less material use, less clogging and sticking in microfluidic settings, and less particulate contamination in larger experiments, such as wind tunnels.

1.3 Review of volumetric velocimetry techniques

Two-dimensional techniques described so far can only provide velocity field within a slice of the entire flow domain. Out-of-plane motion of tracers is a common problem, diminishing the validity of the calculated two-dimensional velocity fields [59], [38]. To obtain a more extensive information on the flow, three-dimensional particle velocimetry methods have been developed. It is customary to describe the dimensionality of velocimetry setups using the pattern $x\text{D}y\text{C}$ where x stands for the number of dimensions of space in which the velocity vectors are obtained and y is the number of obtained vector components. Of particular interest to this report are so-called volumetric velocimetry techniques (3D3C) capable of measuring full velocity vector in the entirety of the flow volume. Designs with a single camera and multiple cameras are available. Single-camera setups are typically cheaper to build

and are preferable in the settings where only a limited visual access of the domain is available. It is also free of errors from mutual misalignment of the cameras [60]. Such techniques rely on decoding the depth of tracers from some imageable property like the amount of defocusing or astigmatic shape deformation. Blurring can be either described analytically [61] or, more simply, calibrated for [62], [20]. Since defocusing occurs on both sides of the focal plane, we cannot uniquely relate it to depth without certain modifications. To that end, Fuchs et al. [20] recommend positioning the focal plane above or below the measurement volume and note a quadratic fall-off of SNR and, alongside it, accuracy with distance from the focal plane. Another class of defocused velocimetry employs aperture masks, typically with three pinholes [63], [64], [65], [6]. Such a mask for a single particle produces a triplet of particle images whose size is used to infer the distance from some reference plane. The advantage of the method is that when the particle crosses the plane, the triplet is flipped allowing depth reconstruction to be unambiguous. Low seeding has to be employed to minimize the overlap, the issue which has been addressed in [66] by using separate CCDs to capture each part of the triplet. Tien et al. [57] note that such a system is hard to setup and calibrate and suggest a different approach wherein the pinholes are equipped with color filters, allowing to discern overlapping particles based on the unique colors produced in the overlap regions. This approach can significantly increase the viable seeding density while still utilizing only one camera. The aperture-based defocused imaging tends to produce low SNR.

Backlit systems have been reported to alleviate this problem [67].

Another widely-used single-camera technique uses astigmatism and deduces depth from the shape of particle images. There is a number of ways to generate this effect, such as bent dichroic mirrors [46] camera tilt [68] and cylindrical lens [69], [60], [53], [70]. Approaches based on this type of lens aberration offer an advantage over aperture-based defocused methods in that much greater SNR can be achieved [46]. Single camera 2D2C velocimetry setups are typically easily converted into the astigmatic mode. The method has found a wide application in micro-scale studies [53] with larger studies also done [68], [71]. Quantitative comparison of astigmatic velocimetry to other 3D3C techniques [60], [71] showed that a comparable accuracy can be achieved. For guidelines of optimal design of an astigmatic velocimetry setup the reader is referred to [72].

Originally multiple-camera techniques, such as Stereo PTV and Tomographic PIV, likewise, can be realized using a single camera with an assembly of prisms [73] and/or mirrors. In that case, the multiple views are either overlaid or are recorded onto different parts of the sensor [74], [75], [76], [24], [77]. An array of mirrors arranged in an ellipsoidal shape was used by Maekawa et al. [78] to capture tracers from up to 80 different views producing high accuracy of Stereo-matching and 3D reconstruction. This method, referred to as multiple-eye (ME) PIV, can potentially perform tomographic PIV.

Holographic imaging is based on recording the interference pattern of the light scattered from the tracers and the reference beam. The resulting col-

lection of the interference fringes contains 3D information of the scene and can be used to calculate volumetric velocity fields. High resolution image-receiving medium is needed for the process which is why transferring the technology to the digital mode requires some trade-offs such as smaller observation volumes. [38], [79]. In the past decade, digital holographic PIV and PTV have found wide application at microscopic scales, since pixel size requirements are less prohibitive in that case [46]. Fahringer et al. [80] and Skupsch et al. [81] used plenoptic cameras for volumetric velocity measurements. Plenoptic cameras are built to capture not simply the amount of light hitting the sensor but also its direction or, in other words, the light field. This is accomplished by mounting an array of microlenses over the sensor. One of the peculiar corollaries of this is that the image can be refocused after being captured. Since, effectively, the camera produces a number of views from different angles, Fahringer et al. [80] applied tomographic PIV processing algorithms to the data and obtained velocity field of a low-Reynolds flow in the wake of a cylinder. They point out the trade-off between angular and spatial resolution as one of the main downsides of the technique. Chen et al. [82] analyzed the multiple-view data from a single plenoptic camera in the 3DPTV framework investigating a steady-state flow in an engine.

Laser-scanning single-camera velocimetry described in [83] relies on measuring 3D2C data on a number of planes and then using incompressible continuity equation to calculate the out-of-plane component. The authors indicate that this approach needs the thickness and spacing of the measure-

ment planes to be small enough to capture the flow structure of interest. A large number of thin planes slows down the measurement, thus leaving the technique qualified for either small volumes or slow flows. Hoyer et al. [84] use a laser-scanning approach with a high-speed camera to image flow in a water tank but applies PTV algorithms to obtain the velocity field. Similar approach was used by Krug et al. [77] who conducted simultaneous volumetric PTV and LIF in a gravity-driven flow. At microscopic scales confocal microscopes equipped with spinning Nipkow discs are well fit for scanning velocimetry. This approach has been used by Kinoshita et al. [11] and Oishi et al. [10] to obtain 3D2C data and calculate the out-of-plane velocity component analytically. The scanning techniques described above offer a tackle to a very prominent problem in velocimetry, the problem of overlapping tracer particles [83].

A different approach in encoding depth is offered by the so-called Rainbow PIV [42]. Depth here is encoded in color. This is achieved by placing a variable-wavelength color filter in front of a collimated white light source. To make sure that all the colors are properly focused on the sensor, a Fresnel phase plate is included in the optical setup of the camera objective. Earlier, McGregor et al. [85] described a similar approach generating a variable-wavelength light via Raman Scattering in glass fiber. Aguirre-Pablo et al. [86] used a light source with an intensity gradient to encode depth.

Dual-plane PIV is designed to measure a full 3-component velocity vector field, but only at two parallel measurement planes. Each plane is viewed by a

dedicated Stereo-pair of cameras and is illuminated by a thin light sheet. The knowledge of velocity in the two planes allows reconstruction of full velocity gradient. In order to avoid cross-registration of particle tracers between the cameras, orthogonal polarization or lasers of different wavelengths are used for each of the measurement planes [87].

It has been noted that velocimetry systems based on a single plenoptic camera suffer from low angular resolution. La Foy et al. [88] have extended the setup and the reconstruction algorithm to several cameras. Their simulations have shown, however, that extending the setup beyond two cameras will not yield a significant improvement in data quality.

Single-camera scanning technique, discussed above, has been combined with Stereo-PIV, one of the more established, commercially available technologies. A Stereo-PIV system usually consists of two cameras focused on a common measurement plane. The velocities measured in the two images are combined to produce 3D vectors. The information produced by Stereo-PIV is of type 2D3C, i.e. full 3D vectors are resolved but only in a single measurement plane. Scanning technology allows augmenting this method to full 3 dimensions [83], [52]. The downside of the technology is a high cost of hardware and limited scanning speeds which may not suffice for fast, unsteady-state flows [80]. Likewise, the problem of short exposure times comes into play in higher-speed systems [89].

Tomographic velocimetry is one of the latest major advancements in the field of velocimetry [90], [91]. Tomography requires a greater number of

cameras (usually around 6) than other multi-camera methods and makes use of the known algorithms such as MART (Multiplicative Algebraic Reconstruction Technique) to reconstruct the light intensity field within the measurement volume. After the reconstruction, known PIV or PTV [92], [25] algorithms are applied to the intensity fields to cross-correlate the two 3D images and calculate the velocity field. Tomographic methods offer a great advantage in seeding (and, therefore, data) density. This, however, comes at a cost of an increased number of cameras. Among the challenges of the tomographic approach are spurious particles in the reconstructed volume called ghost particles and higher equipment cost compared to other techniques. The simplest way to reduce the number of ghost particles is by intensity and size thresholding, since they tend to be dimmer and smaller than their valid counterparts. This is often not optimal, since the true particles are lost alongside. In time-resolved PTV, multi-frame tracking can be used, since ghost particles fail to produce a prolonged trajectory. An Eulerian analog of this was described by Novara et al. [93].

A significant improvement in allowable seeding densities was made possible due to Iterative Particle Reconstruction (IPR) [94]. IPR starts with a standard triangulation. The initially reconstructed particles are then back-projected to the image planes of the cameras and compared to the recorded images to produce residual images. The residual images provide information about obstructed particles which are further triangulated. This iteration is repeated revealing new overlapping particles and removing the ghosts. IPR

requires at least 3 cameras and information on Optical Transfer Function which can be recovered via calibration from experimental images. Building on IPR is Shake-The-Box framework which incorporates temporal data into the analysis using previous frames as a predictor and optimizing the position of a particle by minimizing the residual image (so-called “shaking”). Currently, hardware limitations, namely, image recording and transfer rate limit the application of the classical STB to slower flows with areas such as aerodynamic tunnel testing necessitating modifications [95], [38].

Stereo-PTV is one of the earliest methods for finding 3-dimensional velocities. The method dates back to Chiu et al. [96] who used two film cameras and a stroboscope to study dissipation rates in a steady-state jet flow. Later, a digitized version of the technique allowed full automation, from particle detection to velocity reconstruction. Nishino et al. [97] compared velocity measurements with their 3-camera PTV setup with a digitizer in a Couette flow to the analytical solution. Two camera configurations are usually singled out in Stereo-imaging: translation and angular. In translation setup both cameras are facing the same direction, whereas the optical axes of the cameras in an angular setup converge. While translation setup is easier in its implementation, it suffers from restricted overlapping FOV and inferior image quality, since the overlapping area is imaged off-axis where distortions are greatest [98]. There is no such problem when it comes to angular setups, however, due to perspective and non-orthogonality of the optical axis to the measurement plane, this approach requires a more involved calibration pro-

cedure. An in-depth description of an automated 3-camera 3DPTV system can be found in [99] and [100] who extensively discuss multi-frame tracking and measurement in multimedia environments. The latest advancements in Stereo-PTV include particle tracking through curved interfaces [76], IPR and STB.

Some of the described techniques have been combined to achieve better measurement accuracies. The most natural combinations use PIV as a predictor and PTV as the corrector [54], [101], [102]. Bao et al. [103] use defocusing particle radius to aid Stereo-matching and 3D reconstruction.

Finally, most of the techniques described here have been extended to microscopic scale. A good review of microscale velocimetry methods can be found in [46], [104].

1.4 Velocimetry in the presence of refractive interfaces

Velocimetry in liquids is of special interest to industry and science due to an overwhelming number of processes taking place in liquid flows. The key challenge in multimedia imaging is the presence of refractive interfaces which refract the propagating light and produce distortions in the images [105]. This leads to a breakdown of the linear models based on epipolar geometry, since the epipolar lines used for feature matching and triangulation are replaced with curves [99]. Besides, the presence of a refractive interface even of optical-grade quality will introduce errors into the measurements due to degraded image quality [106]. A large body of work on this has been done

within the underwater photogrammetry community [107], [108]. Only in the 90s, have these results started being transferred to the domain of velocimetry [100], [99].

In later sections, we will offer our means of tackling the problem. Here we will review some of the methods presented in the literature. Probably the simplest way is simply ignoring the refractive interface [109], [110]. This approach is applicable only if very rough data is needed and is not generally used. Giardino et al. [111] used calibration performed in air to quantify errors of Stereo-PIV at millimeter scale. They found that the errors were typically of the order of one micron, however we think that the approach used does not truly reflect z-axis particle motion in a real experiment. The authors used a solid block consisting of stacked glass substrates with the particles sandwiched between them. The test block was traversed in different directions and the measured motion of the particles was compared to the known movement of the block. Thus, the movement of the particles along z-axis is accompanied by the movement of the refractive interface which is not representative of what happens in a typical liquid velocimetry experiment. We have performed preliminary 2D modelling of the errors and concluded that ignoring the interface will introduce critical amount of error into the measurements. In the domain of underwater imaging, it is common to let the refraction effects be absorbed by the standard parameters of a camera model during calibration [112]. Mostly, it is the principal distance and the nonlinear radial and tangential distortion parameters which are modified to

account for the refraction. However, as noted by Shortis et al. [113], the absorption approach is only approximate and will lead to systematic errors. Corrective optics and hemispherical dome ports for camera lens [114], [115] are also frequently employed together with standard calibration techniques to reduce the remaining errors. There has been a limited number of attempts to use corrective optics for velocimetry [116]. We could not find any reports of dome ports used in velocimetry applications. This is possibly due to the large size of the domes. Since they need to be submerged into the liquid, it may be challenging to design a flexible experiment avoiding flow disturbance from the domes. Nishino et al. [97] did not resort to domes but simply submerged the waterproof camera objectives into the liquid to study Couette flow. One potential disadvantage of this approach could be the fact that lenses are usually designed to work in air which could introduce additional aberrations degrading the quality of the image.

By far the most popular method in multimedia velocimetry is orthogonal imaging [117], [52] [118], [119], [120], [24]. The obvious advantage of the method is that it allows minimizing (but not eliminating) the distortions due to refraction. Some studies choose to ignore the remaining error altogether [121], [122]. Refraction can be eliminated if object-space telecentric lens are used, as, for example, in [120], [123]. Otherwise, the distortion still needs to be calibrated for. In the cases where the flow chamber is filled with air, the refraction may be ignored provided the walls of the flow chamber are sufficiently thin [124]. Hori et al. [52] use a polynomial function to cali-

brate for the refraction effect in their orthogonal imaging setup. Orthogonal imaging has been used for single-camera velocimetry as well. Pereira et al. [125] incorporate refraction correction into defocusing PTV and Cierpka et al. [60] take the refraction effects into account when calculating the analytical relationship between particle shape and location for their astigmatic velocimeter. Rossi et al. [126] use a refraction correction to DOC of μ PIV for their topography measurements, while Yoon et al. [127] adjust for refraction in their 3-pinhole defocusing velocimetry experiment.

It is not always feasible to set up an orthogonal imaging experiment. We are further going to review studies where the optical axis of the camera is positioned at an angle to the interface. One suggested solution to the problem is the use of auxiliary prisms which essentially turn the imaging setup into an orthogonal one [128]. A similar approach was adopted by van Doorne et al. [129] to study turbulent flow in a circular pipe. Manufacturing and setting up such a prism-assisted system may be challenging, and many studies have instead opted for calibrating for the effects of refraction. The problem of calibration is simplified if it can be performed within the measurement domain mimicking the experimental conditions. Luthi et al. [130] used a volumetric target with 36 markers placed in the measurement chamber. To study flow in a silicone replica of an aorta, Gulun et al. [131] used a portable 2-point target (“dumbbell”) moving it in the measurement chamber filled with the experimental liquid with a matched refractive index. Kieft et al. [132] and Dore et al. [133], to calibrate their centimeter-scale velocimetry

experiments traversed a known calibration target through the measurement volume at experimental conditions. Similar examples can be found at microscopic scales. Kim et al. [134] sustained a liquid film between the glass substrate and the calibration target. Similar strategy was adopted by Tien et al. [57]. Bown et al. [135] used a separately manufactured micromodel with a pattern imprinted on the bottom wall to calibrate their micro stereo system with the working liquid present. Ideally, we would have the patterns placed at a few depths within the model, however, in the study, the authors assume that placing a pattern at a single depth would averagely represent the refraction effects. The obtained rough PIV measurements were further used as initial guesses for the 3DPTV algorithm. This strategy is often referred to as super-resolution PIV [49].

Such mimicking calibration described above is computationally convenient, since no direct modelling of refraction phenomena is needed. Moreover, Maas et al. [99] argue that such in-situ calibration would provide the highest accuracy, since models cannot capture the idiosyncratic imperfections of a given experimental setup. However, this approach is not always possible to implement due to lack of control and freedom of movement of the target within the measurement domain [136]. This led to the development of frameworks where refraction effects are explicitly included in the model. Most notable work in this area has been done by Kotowski [108] who incorporates the multimedia scenario into bundle adjustment. Maas et al. [76], [99] are credited with adapting the work done in the photogrammetric community

to the needs of velocimetry. In [99], the authors explore the most relevant setting where 2 planar refractive interfaces (3 media) are present. In many cases these are air-wall and wall-liquid boundaries. The effect of refraction here is modelled in the form of an additional horizontal radial shift away from the nadir of the camera. This radial shift is incorporated into the linear model adjoined by a nonlinear lens distortion polynomial and an affine transformation. The method, however, is not tied to the pinhole model. Lindken et al. [89] used the 3-media model with a polynomial mapping function [137] to correct the calibration done in air by vertically traversing a known target. Scanning Stereo-PIV measurements were then performed and validated in a T-junction micromodel. Planar self-calibration [138] was used to correct the discrepancy between the positions of the calibration target and the laser light sheet.

Tracking of unsteady surfaces and velocimetry through changing refractive interfaces [139], [15] constitute a separate domain not covered further in this report.

2 Hardware setup

The 3DPTV setup is schematically shown in Figure 1. The microfluidic chip is placed on a z-translation stage (Edmund Optics) whose motion is measured by a high-accuracy contact sensor (Keyence GT200). The chip is illuminated by a double-pulse 200mW 532nm Nd:YAG laser (Quintel Ever-

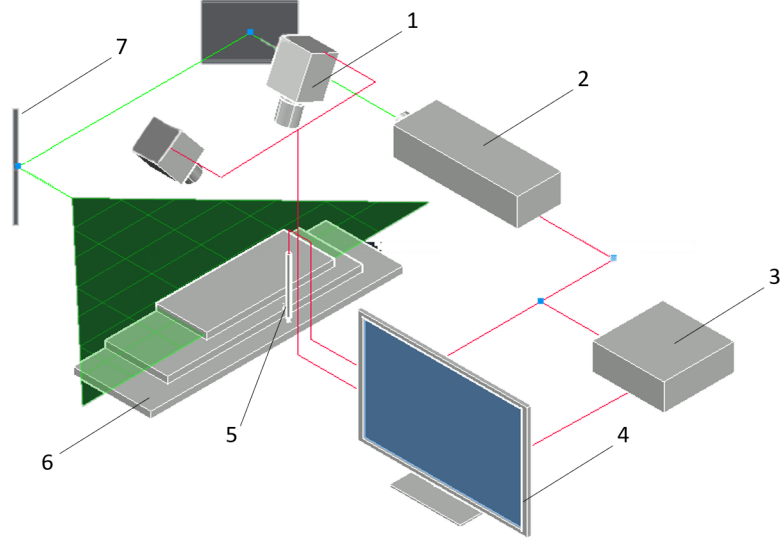


Figure 1: 3DPTV hardware setup. 1 - cameras, 2 - laser, 3 - Synchronizer, 4 - PC, 5 - displacement sensor, 6 - z-translation stage, 7 - system of mirrors (light guide arm.)

green) and imaged by two cameras (29MP Powerview, TSI inc.). The cameras are positioned over the chip on a support frame allowing translation in all three directions. Custom tilt of the camera bodies is provided by rotary stages (Edmund Optics), and perspective-control macro lens (Nikon PC-E Micro-Nikorr 45mm $f/2.8D$ ED) with long-pass 550nm cut-off optical filters (Edmund Optics) are used to capture the red fluorescent light of the tracers ($12\mu m$, FluoroMax) or a fluorescent dye. The perspective-control objectives orient the camera optics in accordance with the Scheimpflug and the hinge rules [140]. The objectives are separated from the object plane by about 150mm. We achieve an FOV of about $200 \times 130mm^2$. The laser beam is

conducted to the chip via a guide arm (LaserPulse™, TSI inc.). Before hitting the chip, the beam is shaped by two concave (15mm and 25mm, Edmund Optics) and one convex (300mm, Newport Corporation) cylindrical lens. The concave lens fan out the beam and the convex one focuses it into a horizontal sheet of adjustable thickness. The beam-shaping lens array is placed on a jack stage enabling control of tilt and z-position of the light sheet. The timing of image capture and laser emission is controlled by the Synchronizer unit (TSI inc.) and is programmed through commercial software (Insight 4G, TSI inc.). Constant-rate syringe pumps (Harvard apparatus) are used for fluid injection with back-pressure kept at the atmospheric mark. All the components of the setup, except for the laser and the pumps, are enclosed in a box made of opaque acrylic plastic. This helps considerably improve the Signal-to-Noise Ratio (SNR) by blocking out the ambient light. Calibration is performed using a flat target (Max Levy Autograph, Inc.) with a square grid of white dots on a dark background. The target is illuminated by a simple LED lamp. The calibration, image processing, Stereo-matching, 3D-reconstruction, and temporal matching are done with the help of an in-house software implemented in MATLAB.

Also, two chips have been manufactured by casting polyurethane resin: simple, parallel-wall $180 \times 90 \times 0.794mm^3$ Hele-Shaw and a replica of a stress-induced fracture. The error of the height of the Hele-Shaw chip is $\approx 40\mu m$ or 5% and is determined by the manufacturing tolerances. The microfluidic chips are each equipped with 3 inlets and 3 outlets tapping into the inlet

and outlet manifolds. The manifolds serve as a flow distributing system and also help establish uniform solute concentration front for step-injection solute transport experiments. The symmetric design of the chip allows investigation of the solute transport in both directions for the same fracture sample.

We use custom-made (Cargille Labs) silicone oil with a refractive index matched to the one of the polyurethane resin ($n=1.4997$) as the experimental liquid. Matching the refractive index eliminates the need for detailed knowledge of the geometry of the upper wall roughness of the chip and helps avoid complex data processing in that regard.

2.1 Microfluidic chips

Microfluidic chips were manufactured via casting clear polyurethane resin (Crystal Clear 200, Smooth-On) in silicone molds (Mold-Max 30, Smooth-On). For simple Hele-Shaw chips, the silicone molds were prepared by casting in polystyrene molds we manufactured. For the fracture replicas a $10 \times 6 \times 12inch^3$ block of Clashac sandstone was first cut. The block was put into a hydraulic press with two metal rods placed above and below the block, and a stress-induced fracture was then generated. The extra sandstone was trimmed away to end up with $8 \times 4 \times 0.5inch^3$ slabs which were then used together with auxiliary polystyrene parts to cast the silicone molds for the top and bottom plates of the fracture replica. Finally, the top and bottom pieces of the chip were cast in the silicone molds. In preparing the chip close attention should be drawn to the surface quality of the top face which is being

imaged by the cameras. To avoid surface rippling and large-scale undulations and to minimize air bubbles, the following casting procedure was adopted. The two parts of the casting resin are weighted and then thoroughly double-mixed wherein in the middle of the process the whole mixture is poured from one mixing vessel into another. The mixed resin is poured into the silicone mold and cured in a pressure chamber at ambient temperature and 110 psi for at least a week. The cured product is then placed into a convection oven at 45 °C. Care should be taken so as not to bend the chip in the process of the transfer. The heat post-cure lasts at least three days. The finishing stage includes installation of the inlet and the outlet ports and bonding of the top and the bottom plates. The casting resin itself is used as the bonding agent which keeps the optical properties consistent throughout the chip. The laser light is fed through the side of the chip, therefore, to maximize the delivery of the light to the particles, it is important to have that side of the chip clear and smooth. This light-receiving side is created during an additional step after the bonding is complete. One of the common problems of casting is the formation of meniscus in the three-phase contact line where resin, silicone, and air meet [141]. To prevent this issue, initially we cast a larger piece than projected and then trim off the edges with the meniscus curvature. This way, however, is not as practical for the rock-replica models, therefore, subsequent manual beveling of the edges is performed instead. The chip surface quality is evaluated via visual inspection.

2.2 System aligning and focusing

Prior to any measurement, system alignment, focusing and calibration need to be completed. We start by filling the chip with the working fluid. It is important to avoid bubbles in the system. We achieve this by keeping the model tilted during the flooding. Next, we level the sensor deck and fasten the chip on the chip deck (Figure 2). After the chip is mounted, we adjust the focus of the cameras. Focusing cameras with tilt-shift lens and a fixed position in space involves 3 key variables: sensor tilt, lens tilt and, finally, the lens focus setting. An even greater challenge is posed by the fact that the focus should be obtained within the microfluidic model which is located behind the refractive air-plastic interface. This means that the settings obtained by focusing on a given plane in air in general will not produce an optimal focus at the same plane when submerged in liquid. To aid focusing in the presence of the refractive interface, we added marker crosses on the bottom wall of the chip. Both cameras have same, fixed

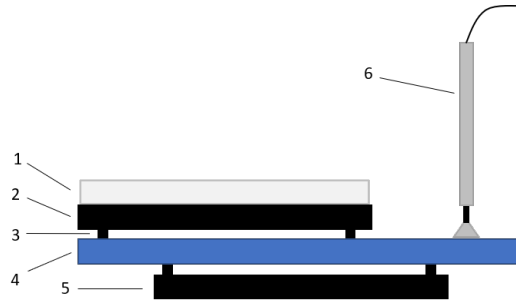


Figure 2: Z-stage where the microfluidic chip resides. 1 - microfluidic chip, 2 - chip deck, 3 - levelling screws, 4 - sensor deck, 5 - z-translation stage, 6 - displacement sensor

but opposing sensor tilt leaving only two variables to tune. Adjusting the remaining parameters to obtain the perfect focus may still be tedious which is why we have devised a handy shortcut which allows us to arrive in the vicinity of the perfect focus. Provided that we start with the FOV centered around the model, first, adjust the lens focus until the middle of FOV is in focus. Now start adjusting the lens tilt. This should bring the whole desired plane approximately in focus uniformly. Little parameter adjustment is needed after that.

3 Calibration

An accurate camera calibration is the most important prerequisite for a successful velocimetry experiment. A massive amount of literature in photogrammetry and computer vision has been dedicated to the problem of calibration. The process of calibration is concerned with obtaining the so-called extrinsic (rotation, position) and intrinsic (principal distance, principal point, skew, aspect ratio) parameters of the cameras in the imaging setup. It is usually done using a known target imaged at several positions (bundle adjustment). In contrast, self-calibration (or auto-calibration) makes few or no assumptions about the structure of the scene [142] often delivering the camera parameters from images of primitives or point correspondences [143]. Among the limitations of self-calibration has been the fact that a lot of the development work is centered around linear camera models [143] and the lack

of scale among the obtained parameters [144].

3.1 Review of camera models

In a mechanistic calibration, camera model plays a central role. There have been a number of models suggested, and those will be discussed below. Pinhole camera model is used most widely for its simplicity and mathematical convenience. The model mimics camera obscura and maps the physical space onto the image plane through the center of projection playing a role of the pinhole. Pinhole model is often adjoined by a distortion model usually comprising radial and tangential components. Radial distortion is assumed rotationally symmetric and is either pushing the image points outward (barrel distortion) or pulling inward (pincushion distortion). Tangential distortion is not in general symmetric and arises due to imperfectly aligned lens elements. These distortion modes are usually modelled with a polynomial [107]. A common disadvantage of such models is limited invertibility [143] which led to some researchers using only a single polynomial coefficient [145]. There have been attempts of using the pinhole camera model in a Scheimpflug setting. Cornic et al. [146], Fournel et al. [147], and Kumar et al. [148] have used an intermediate tilted image plane to model the lens tilt. Nocerino et al. [149] used an additional distortion term called the affinity factor to correct for the optical axis of the camera being non-orthogonal to the sensor. This approach is simple however offers limited accuracy. In computer graphics, further extensions in the form of thin-lens approximation are used to model

the amount of defocusing [150]. Sturm et al. [143] offer a comprehensive review of the vast diversity of camera models available including the models for wide-angle (fish-eye, catadioptric) and zoom lens. They classify the models into global, local and discrete. Global models assume a camera model for the whole imaged physical space. Local methods allow for a variation of the model from region to region. Two-plane model [151] is an example of a local model which relaxes the assumption of central projection. The model uses at least two images of the known calibration target separated vertically (hence the name) to reconstruct the 3D rays corresponding to each point in the image plane. The 3D rays are not forced to intersect at the same point (center of projection). Martins et al. [151] suggest using a linear spline for the interpolation in between the calibration data to cover the survey area. Similar approach can be found in [152]. Finally, discrete models aim to model light rays discretely for each pixel (raxels) [153].

In an excellent paper, Steger [144] building on the work of Kumar et al. [148] has developed a versatile camera model capable of handling a spectrum of tilt and rotation settings of an objective. He shows that the pinhole camera model fails to accurately model the imaging rays when tilted lens are used and thus will produce subpar results for the cameras with perspective control (tilt-shift). His work is based on a thick-lens approximation which is capable of modeling an assembly of lens. He also analyzed the degeneracies of the model and presented calibration results for some well-known objectives, incidentally, including the Nikon PC-E Micro-Nikorr 45 mm f/2.8D ED used

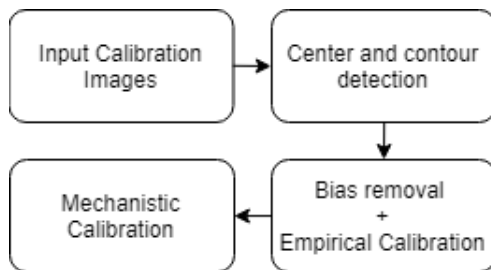


Figure 3: Calibration workflow

in our study. The objective was reported to be image-side telecentric. More recently, Sun et al. [154] have conducted an experimental comparison of Scheimpflug camera models and the General Non-parametric Model [152]. The pupil-centric model developed by Steger has been shown to be at least as good as the other models in every test. Since the testing had a lack of clarity of the ground truth, and since in our application we are interested in the correct modelling of the 3D image rays, we have decided to employ the more rigorous model of the tested, the Steger pupil-centric model. Below, we are going to present a novel calibration method tailored for velocimetry through a refractive interface using a known calibration target. Before dissecting the computational side of our calibration, let us look at the calibration protocol.

3.2 Calibration protocol

After the focus is obtained, the stage is lowered by the amount equal to the thickness of the calibration target (3.2 mm for this study), and the target is placed on top of the chip. The chip deck (Figure 2) is then oriented to

bring the target to a level position. Such an approach eliminates the effect of possible non-uniform thickness of the chip and ensures that the target movement between the calibration image captures remains perpendicular to the target itself. Here we are assuming that the calibration target has a uniform thickness. By default, we capture images of the target at 3 positions (planes) along the z-axis. The first plane is important since it is the future position of the refractive interface. We will denote this plane as π . The other two calibration planes are located below and above the first plane. We usually capture 80-100 images per position to minimize the effect of the image noise and maximize the accuracy of feature detection. We make use of k-means clustering to identify the same calibration dots across the images.

The workflow of the calibration algorithm is depicted in Figure 3. The calibration script begins by a GUI input of the calibration images. Next, the images are masked and binarized. We found that while a global threshold works better for experimental images, for calibration images due to variable illumination adaptive thresholding [155] is a preferred choice.

The batches of images are analyzed by our calibration script which starts by detecting the centroids and contours [156] of the calibration dots. The detected dots and contours are then arranged in the correct order corresponding to the array of physical coordinates. Poor quality edges and undetected points are rejected for higher data reliability. It is known that using circular markers for calibration leads to bias arising from perspective and distortion [157], [144], [158]. Based on the work of Heikilla et al. [157], we have devel-

oped a rigorous procedure for the correction of the bias using the detected contours. The correction procedure is iterative and is performed simultaneously with the empirical calibration (described below). The effects are corrected not just for the first (plane π), but for all the target positions. The details of the procedure can be found in Appendix A. Added benefit of this approach is that data points with unreasonable perspective/distortion bias can be excluded from the dataset as outliers. This further improves the quality of the calibration data. Finally, for each camera k we now have an ordered array of corrected image position vectors $\mathbf{X}^{(k)} \in \mathbb{R}^2$ corresponding to the position vectors in the physical space $\mathbf{x} \in \mathbb{R}^3$. We are ready to begin the calibration.

Our calibration consists of two main parts: 3D mechanistic and 2D empirical, both having their own advantages. An optional self-calibration procedure will also be described.

3.3 Empirical model

The empirical approach is based on the work by Soloff et al. [137] which is widely used in velocimetry, albeit used differently than here. Each imaged horizontal plane is calibrated for separately. If a point with position $\mathbf{x} = [x_1 \ x_2]^T$ on a given plane α in physical space is imaged onto position $\mathbf{X} = [X_1 \ X_2]^T$ in the image space, we can write the empirical model the following

way:

$$\mathbf{X} = \begin{pmatrix} \mathbf{a}(\mathbf{x})^T \mathbf{b}_1 \\ \mathbf{a}(\mathbf{x})^T \mathbf{b}_2 \end{pmatrix} \quad (1)$$

where $\mathbf{a}(\mathbf{x})$ is a vector of the form:

$$\mathbf{a}(\mathbf{x})^T = [x_1^7 \ x_2^7 \ x_1^6 x_2 \ x_1 x_2^6 \ x_1^5 x_2^2 \ x_1^2 x_2^5 \ \dots \ x_1^i x_2^j \ \dots \ 1] \quad (2)$$

$$\forall i, j: \ i + j = k, \ k \in \{1, 2 \ \dots \ 7\}$$

and \mathbf{b}_1 and $\mathbf{b}_2 \in \mathbb{R}^{36}$ are calibration vectors to be determined.

3.4 Mechanistic model

The next step is mechanistic calibration which aims at fitting the calibration data (corresponding space and image points) with a physically-justified camera model. We are using a thick-lens-based camera model designed specifically to handle tilt-shift lens [144]. All the formulation will be presented in non-homogeneous Cartesian coordinate system. For better understanding, we offer an illustration of the camera model in Figure 4. To obtain an image by our modelled camera, we start by converting some position vector in space \mathbf{x}_w from the reference frame of the calibration target into the camera reference frame (\mathbf{x}_c). This is done via a rotation (q) and translation (\mathbf{t}) as such:

$$\mathbf{x}_c = q \mathbf{x}_w' q^{-1} + \mathbf{t} \quad (3)$$

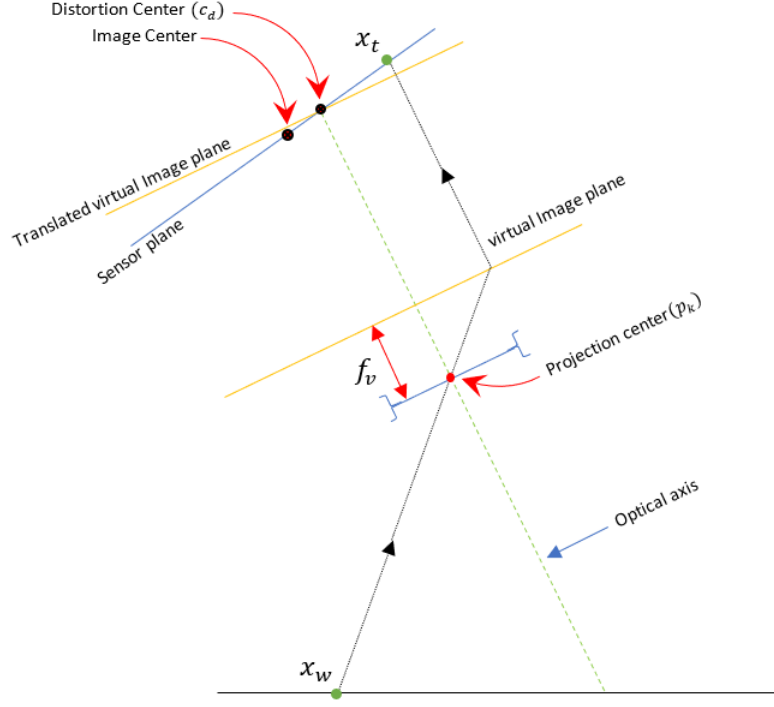


Figure 4: Mechanistic camera model, used in this study.

where q is a unit rotation quaternion and x'_w is a quaternion of the form $(0, \mathbf{x}_w^T)$. We chose to use quaternions over matrix rotations due to a smaller number of redundant parameters, i.e. smaller difference between the number of parameters and the number of actual degrees of freedom. It has been proven by Euler that any rotation in a 3D space can be represented by only 3 angles (Euler angles). Quaternions encode rotation in 4 parameters similar to axis and angle method. The thick lens are handled by introducing a virtual image plane [159], [160] which lets us use simple pinhole projection equations. The virtual image plane is located at a distance $\|f_v\|$ from the projection

center of the camera and is perpendicular to the optical axis (as opposed to the image sensor). Using perspective equations, point $\mathbf{x}_c = [x_{c1} \ x_{c2} \ x_{c3}]^T$ is projected onto the virtual image plane ($\mathbf{x}_u \in \mathbb{R}^2$):

$$\mathbf{x}_u = \frac{f_v}{x_{c3}} \begin{pmatrix} x_{c1} \\ x_{c2} \end{pmatrix} \quad (4)$$

The obtained \mathbf{x}_u is free of lens distortions. We consider only two types of distortion: radial and tangential which are modeled by a polynomial [107] to give distorted virtual image coordinates ($\mathbf{x}_d = [x_{d1} \ x_{d2}]^T$):

$$\mathbf{x}_u = \begin{pmatrix} x_{d1}(1 + k_1 r_d^2 + k_2 r_d^4 + p_1(r_d^2 + 2x_{d1}^2) + 2p_2 x_{d1} x_{d2}) \\ x_{d2}(1 + k_1 r_d^2 + k_2 r_d^4 + 2p_1 x_{d1} x_{d2} + 2p_2(r_d^2 + 2x_{d2}^2)) \end{pmatrix} \quad (5)$$

where k_1, k_2 are radial distortion coefficients p_1, p_2 are tangential distortion coefficients and $r_d = \|\mathbf{x}_d\|^2$. As noted above, such a polynomial model suffers from a lack of analytical inverse. This, however, will not pose a problem due to the way the objective function is formulated later in this section (Equation 11).

Up until now, the lens tilt can be ignored. It has been shown by Steger [144] that such simple pinhole model is applicable to many conventional cameras, unless wide-angle lens is used [143]. Additional considerations must be made if lens tilt is employed. Steger offers separate treatment for entocentric, image-side, object-side and bilateral telecentric lens. As was mentioned, the

study also reports the 45mm lens used in our work to be image-side telecentric. We confirmed this claim by calibrating our cameras using both the entocentric and the image-side telecentric models. For that reason, in what follows, we are going to cover only the image-side telecentric model.

Another distinctive part of the Steger camera model is that camera tilt is defined by rotation around two axes by angles ρ and τ . This is useful when modeling objectives which can both rotate around the optical axis and tilt the lens.

After we have introduced the distortion on our virtual image plane, what remains is to project the resulting distorted image from the virtual image plane onto the real image plane containing the camera sensor. In image-side telecentric camera the light rays hit the sensor perpendicularly. This can be modelled as the following orthographic projection:

$$\mathbf{x}_d = T^{-1}\mathbf{x}_t \quad (6)$$

For the purposes of the calibration algorithm, we give the inverse transformation, converting from the real image plane to the virtual image plane. Here T^{-1} is defined as:

$$T^{-1} = \begin{pmatrix} \cos^2 \rho(1 - \cos \tau) + \cos \tau & \cos \rho \sin \rho(1 - \cos \tau) & 0 \\ \cos \rho \sin \rho(1 - \cos \tau) & \sin^2 \rho(1 - \cos \tau) + \cos \tau & 0 \\ 0 & 0 & 1 \end{pmatrix} \quad (7)$$

In Figure 4, we translate the virtual image plane parallel to itself along the optical axis until the virtual and the real image lines representing the corresponding planes and the optical axis intersect at one point. That point is the distortion center of the image where distortion is null. Notice, that the distortion center of the image does not lie in the image center or the principal point which is defined as the point on the image plane from which a perpendicular can be drawn to the center of projection. Image center, principal point and distortion center tend to coincide within manufacturing tolerances when there is no lens tilt. Tilting of the lens leads to the spreading of the points with the distortion center and the principal point moving in different directions with respect to the image center. Specifically, in the situation depicted in Figure 4, the distortion center is expected to move closer to the top of the sensor and the principal point to slide down below the image center. The expected behavior of the distortion center has been confirmed in this study. Similar conclusions can be found in [161], [162], [163], [149].

Finally, we are only left to convert the obtained real sensor plane coordinates into pixel units. After the orthographic projection onto the real image plane, we get sensor plane coordinates normalized by the geometric position of the distortion center. To arrive at the image coordinates in pixels, we need to scale these by the pixel size and then normalize by the image origin instead:

$$\mathbf{X} = \text{diag}(\mathbf{s})^{-1} \mathbf{x}_t + \mathbf{c}_d \quad (8)$$

where $\mathbf{s} = [s_1 \ s_2]^T$ are the pixel sizes and \mathbf{c}_d are the coordinates of the image distortion center in pixels.

In our calibration algorithm we are interested in the inverse of the equation above which is trivial to derive.

3.5 Empirical calibration algorithm

The \mathbf{b}_1 and \mathbf{b}_2 in the empirical model 1 are found the following way:

$$\mathbf{b}_1 = A^\dagger \mathbf{X}_1$$

$$\mathbf{b}_2 = A^\dagger \mathbf{X}_2$$

where A^\dagger is the Moore-Penrose pseudo-inverse of matrix $A = (\mathbf{a}_1 \ \mathbf{a}_2 \ \dots \ \mathbf{a}_n)^T$, $a_i = a(\mathbf{x}_i)$ (Equation 2), with \mathbf{x}_j being the position of particle i on plane α and $\mathbf{X}_1 = [X_{11} \ X_{21} \ \dots \ X_{i1} \ \dots \ X_{n1}]^T$. \mathbf{X}_2 is defined in similar way.

We found that increasing the order of the mapping beyond 7 does not improve the accuracy. For each camera the polynomial fit is performed via a quick linear regression separately for each calibration plane. MATLAB uses Singular Value Decomposition to compute the pseudo-inverse. This alleviates conditioning issues, however, may still fail for such high powers. It is therefore important to scale and shift the pixel and physical space coordinates before computing the pseudo-inverse. For camera k , we can denote the obtained mappings as $I^{(k)} : \mathbb{R}^2 \rightarrow \mathbb{R}^2$ for forward-projection and $I^{(k)-1} : \mathbb{R}^2 \rightarrow \mathbb{R}^2$ for the back-projection. Thus, for camera k , plane α , we have two mutually

inverse mappings:

$$\mathbf{X}_{\alpha}^{(k)} = I_{\alpha}^{(k)}(\mathbf{x}_{\alpha}) \quad (9)$$

$$\mathbf{x}_{\alpha} = I_{\alpha}^{(k)-1}(\mathbf{X}_{\alpha}^{(k)}) \quad (10)$$

$$\mathbf{x}_{\alpha} \in \alpha$$

The obtained maps are nothing else but a highly accurate two-way camera model for specific planes in space. We use this model in the simultaneous empirical calibration coupled with bias correction, as discussed above and, in closer detail, in Appendix A. We will also use the empirical model to find the correct z-position for the microfluidic chip post-calibration, triangulation, estimation of lens distortion center and self-calibration as will be discussed further.

3.6 Mechanistic calibration algorithm

Following the work of [164], we split the calibration into two stages: linear and non-linear. Linear stage ignores the lens distortions and the complexity beyond pinhole model. After the linear regression, we obtain estimates of the virtual principal distance f_v and approximate \mathbf{t} and q . The details on formulating the linear problem can be found in [165]. In addition to that, while it is common to take the center of the image as the initial guess for the principal point and the distortion center, as discussed above, those become significantly different in the case of tilted lens. Since we have found that

the tilt-shift lens camera model used here is very sensitive to the initial estimate of the distortion center, we have designed an algorithm to extract the approximate image coordinates of the distortion center. The algorithm is based on the assumption that any line image passing through the distortion center will only be stretched or contracted and not curved [166] (only radial distortion is considered in this simplified case). Using the empirical mapping (10), we back-project an orthogonal line grid from the image plane onto the calibration plane in physical space. We then fit straight lines separately to each line in the grid in the world reference frame and record the error. The distortion center is estimated to be at the point where the fit error attains minimum. It may seem that a more natural way of estimating the coordinates of the distortion center would be forward-projecting straight lines from the physical space. This intuitive approach however did not perform well, due to, what we hypothesize, the break of radial symmetry of distortion when lens are tilted. We have found that using the described back-projected method produced more reasonable results.

Following the linear solution, we perform nonlinear optimization to fit the obtained and corrected calibration data with the mechanistic camera model. We denote the passive transformation of some point in physical space into the camera reference frame (3) followed by perspective projection of the point onto the virtual image plane (4) by $M_{obj} : \mathbb{R}^3 \rightarrow \mathbb{R}^2$. Denote by $M_{img}^{-1} : \mathbb{R}^2 \rightarrow \mathbb{R}^2$ the descaling of the captured pixel coordinates of the point image and normalization by the distortion center (inverse of (8)) followed by

the transformation from the tilted real image plane onto the virtual image plane (6) and undistortion (5). Thus the comparison of the given image coordinates and the ones computed by the model is performed on the virtual image plane. This strategy allows to avoid inverting (5). The resulting objective function will then look like:

$$\epsilon(\mathbf{y}) = \sum_{i=1}^n \|M_{obj}(\mathbf{x}_{wi}; q, \mathbf{t}, f_v) - M_{img}^{-1}(\mathbf{X}_i; k_1, k_2, p_1, p_2, \rho, \tau, \mathbf{s}, \mathbf{c}_d)\|^2 \quad (11)$$

where $\mathbf{y} = [q, \mathbf{t}^T, f_v, k_1, k_2, p_1, p_2, \rho, \tau, \mathbf{s}^T, \mathbf{c}_d^T]$.

It is well-known that the nonlinear fit of camera models often leads to local minima [167]. To tackle this, we use a global optimization technique wherein optimization runs for a specified number of initial guess vectors. The vectors of initial guesses are randomly generated in the allowable parameter space with each parameter bounded by the user within a plausible interval typically centered around the initial guess obtained from the linear step of calibration. The optimization is run in parallel for multiple initial guesses at once and typically takes less than a minute to complete. The solution with the lowest residual error is then chosen. The parallel optimization is performed using *multistart* framework in MATLAB with trust-reflective algorithm (*lsqnonlin* function in MATLAB) running on each thread. For quality check, after the calibration is complete, reprojection error maps are generated for both the empirical and the mechanistic calibrations (Figure 5). Such an error report consists of 3 plots presenting information on the distribution of the direction

and the magnitude of the reprojection errors. Typical RMS error for the mechanistic calibration is around 0.12 px, which is on par with or better than the tilt-shift computer vision application reports in the literature [144], [149], [148]. The takeaway from the mechanistic calibration is the position of the entrance pupil of the camera which serves as the object-side projection center with all the rays converging there. To calculate the position \mathbf{p}_k of the entrance pupil in the calibration reference frame, we use:

$$\mathbf{p}_k = -(q_k^{-1} t'_k q_k) \quad (12)$$

where t'_k is a quaternion of the form $t'_k = (0, \mathbf{t}_k)$. It is important to note that among the model degeneracies reported by Steger are the s_x , s_y , f_v and the f_v , ρ , τ , s_x , s_y . Those parameters cannot all be optimized for at the same time. We solved this problem by running a calibration without a lens tilt ($\tau = \rho = 0$). We have found s_x to be $0.0055mm$ which is exactly the number reported in the documentation of the camera. We thus solve all the degeneracies by fixing s_x .

3.7 Post-calibration protocol

After the calibration is complete, the microfluidic chip needs to be returned into the original position. Otherwise, there will emerge a difference between the real, experimental reference frame in which the measurements are taken and the calibration-established reference frame on which the model is based.

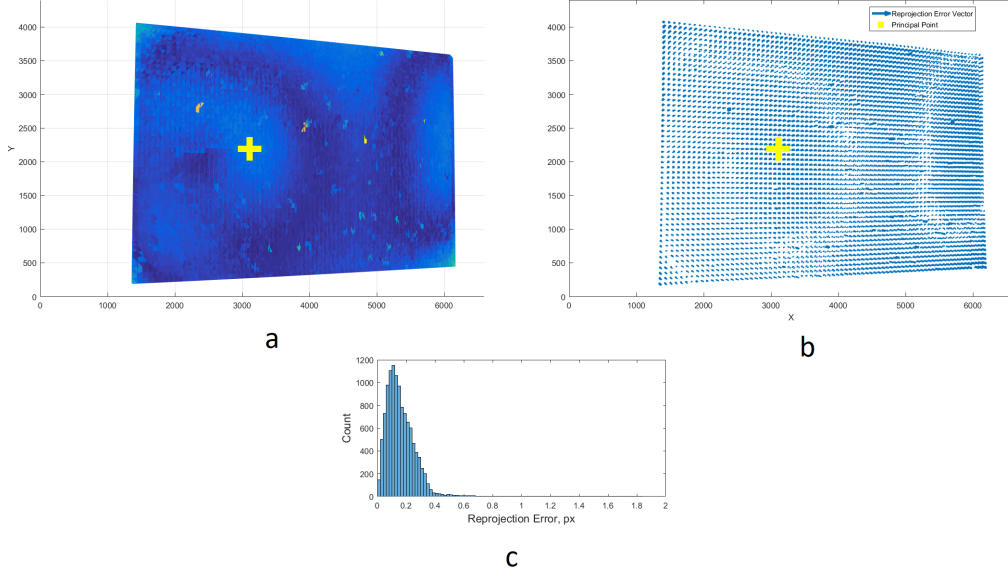


Figure 5: Calibration diagnostics. a) Color-coded map of reprojection error magnitude. b) Vector field of reprojection errors. c) Histogram of reprojection error magnitude. Yellow cross denotes the center of distortion.

In other words, the top surface of the microfluidic chip has to be returned to the same position where the top surface of the calibration plate was during the capture of the first calibration image (plane π). Deviations from that will lead to errors in triangulation. This difference in the reference frames, denoted as dRF , will mostly manifest itself along the z-axis provided the assumption of the uniformity of the thickness of the calibration target holds.

We offer three ways of addressing the problem of finding the correct chip position. First is relying on the measurements of the displacements in between the calibration planes by our displacement sensor and the target thickness measurements by a micrometer. Having all the measurements, we can

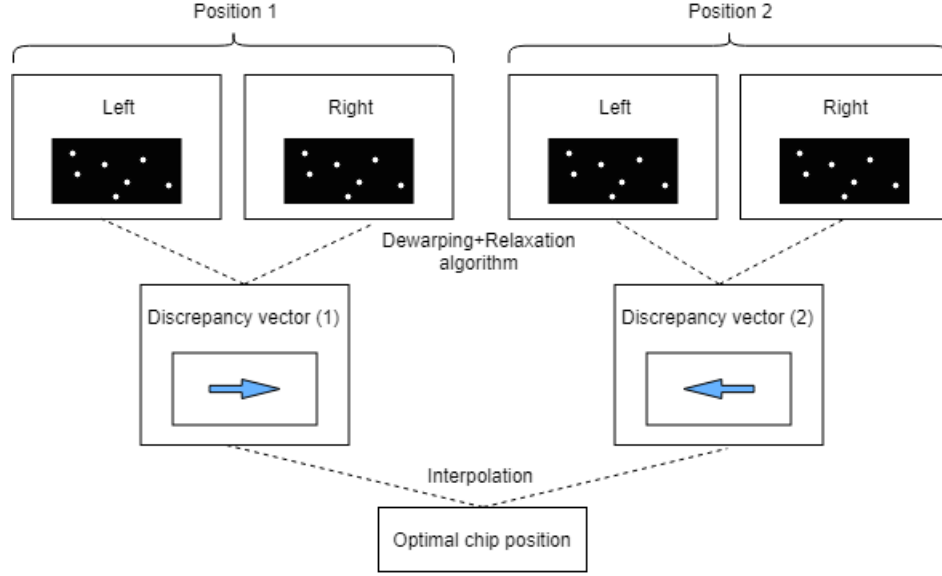


Figure 6: dRF correction flowchart.

calculate the exact position into which the chip needs to be returned. Second is the self-calibration technique which will be described below. Finally, the third way uses the empirical calibration polynomial for plane π into which the top surface of the chip needs to be returned. Let us now look closer at the 3rd approach. To find the correct position for the chip, we place $30\mu m$ fluorescent particles on top of the chip. The best results are obtained with a low-density collection of individual particles. The dry particles are mixed in Methanol and shaken to get rid of chunks. A small droplet of the suspension is then placed in the middle of the top surface of the chip. We let a few minutes for the Methanol to evaporate leaving behind the collection of individual particles resting on top of the model. The particles are imaged in at least two (we usually image at three) z-positions. We grab 80-100 images per

plane to minimize the effect of image noise. The process diagram is shown in Figure 6. The displacement sensor readings are recorded at each z-position. For simplicity, let us look at the case where the particles are captured only at 2 positions. To calculate the optimal position for the chip, we make use of the following rationale. Let us capture an image of a point which lies on the plane π and then back-project the images of the point from both cameras back onto the same plane using correspondent mappings $I_{\pi}^{(L)-1}$ and $I_{\pi}^{(R)-1}$ obtained during the empirical calibration. Let us assume that the mappings are error-free for now. Then we get:

$$I_{\pi}^{(R)-1}(\mathbf{X}^{(R)}) = I_{\pi}^{(L)-1}(\mathbf{X}^{(L)})$$

Where $\mathbf{X}^{(L)}$ and $\mathbf{X}^{(R)}$ are the image coordinates of our point. Now, let us view the case where the imaged point is not located on the first calibration plane but instead is on some horizontal plane π' which is shifted from the first calibration plane by vector \mathbf{dz} along the z-axis. Then, when comparing the back-projected points, we get:

$$I_{\pi}^{(R)-1}(\mathbf{X}'^{(R)}) - I_{\pi}^{(L)-1}(\mathbf{X}'^{(L)}) = \mathbf{d}$$

Where $\mathbf{d} \in \mathbb{R}^2$ is a discrepancy vector whose magnitude is correlated with $\|\mathbf{dz}\|$. We can use this fact by imaging the particles on top of the chip at a few elevations, calculating the average discrepancy vector for each position, and, by interpolation or extrapolation, finding the optimal z-position where

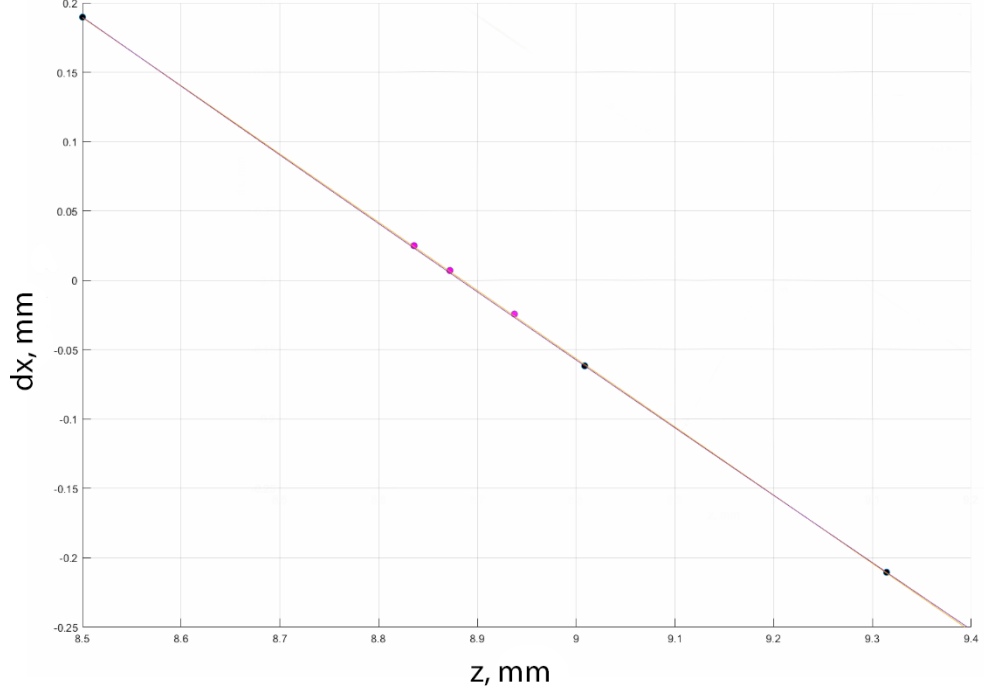


Figure 7: dRF correction plot. Discrepancy vs. the z -position of the chip with dots representing measurements of discrepancy at different z -positions. The optimum position is where $dx = 0$. The data is fit with a linear function.

the discrepancy vector is $\mathbf{d} = \mathbf{0}$. We take into account the finite size of the particles by adding the nominal radius of the particles to the estimate of the optimal elevation.

Let us now discuss how the discrepancy vector is estimated. For a given plane different from π a cluster of particles back-projected using $I_{\pi}^{(k)-1}$, $k = \{L, R\}$ will result in two similar clusters, L and R shifted by the discrepancy vector. We can calculate the average displacement by running relaxation PTV algorithm (discussed in the subsection 5.4) and finding the displacement

vector for each particle in cluster L to its match particle in cluster R . The displacement vectors from all the particles are then averaged to give the discrepancy vector for the elevation. When running the relaxation algorithm, the rigidity radius [168] can be set to a very low value in this case because uniform displacement is expected. Another simple way of doing this would be simply calculating the displacement vector between the centroids of L and R . In Figure 7, we present an example plot of the discrepancy vector (y-axis) vs. the z-position of the chip with the particles (x-axis). We can see how all six dots fall on the same line which indicates the consistency and validity of the method. From the plot, we can read the sensor reading z which gives a discrepancy value of zero along x-axis. In this case, the optimum position is about $8.88mm$. More precise values are reported by the algorithm. For improved accuracy, more iterations can be performed narrowing down the subsequent iterations around the updated estimates of the optimal position. The advantage of this method is that it does not rely on hardware measurements and suffer from accumulated error. Here, the main source of error is the error of finding centroids of the particle images and the error of the obtained empirical mapping.

3.8 Self-calibration

Our self-calibration approach relies on minimization of the residual reprojection error of triangulation as defined in Equation 14. The optimization is performed on experimental data and does not need any object with known ge-

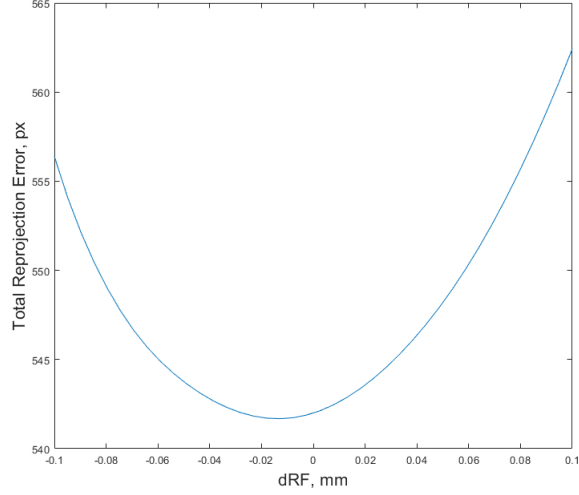


Figure 8: Finding the correct dRF through minimization of reprojection error.

ometry. The self-calibration, however, can only be used to refine the already obtained camera model parameters. Our sensitivity analysis (Appendix B) shows that reprojection error is indeed a good metric to use, since it attains minimum at the correct position of the particle and is concave in its neighborhood. In principle, the self-calibration procedure can be used to correct not only dRF , but also the full position vectors of the cameras. The results of this however were not satisfactory so far, possibly due to interdependence of the camera position parameters with respect to triangulation. Another obstacle may come from the error in the empirical mapping. We, however, achieve a reduction of the errors by 45% in our tests if we optimize the triangulation error varying only dRF (Figure 8). This shows how important the correct position of the chip surface is in our experiments.

All the calibration code is implemented in MATLAB and gathered in one convenient, interactive script.

4 Experimental procedure

Our goal is to validate the 3DPTV setup presented here and a simple Hele-Shaw polyurethane chip is ideal for the purpose. We will be focusing on resolving the parabolic velocity profile. For that purpose, we use a simple setup with a single inlet port injecting into the middle of the inlet manifold and a single outlet opening into the atmosphere. We are injecting silicone oil with a matched refractive index at a constant rate of 0.2 cc/min . For each camera, a 100 image pairs are taken with a Δt of 0.375 s . Before capturing the images, the flow is allowed to continue for a few minutes to let it stabilize. The measurements are assumed to be performed at steady-state conditions. We use straddle imaging regime where two frames (A and B) are taken in a quick succession and a longer interval then follows before another quick pair of frames is captured. This regime is opposed to a uniform frequency regime often employed in particle tracking experiments. For this preliminary validation, we focus on a region of the model spanning $35 \times 30\text{ mm}^2$. Both camera sensors are tilted by nearly 12.5° with respect to the horizontal. The optical axes of the camera thus cross at about 25° . The lens tilts, needed to bring the chip in focus for the left and the right cameras respectively are about 2° and 2.8° .

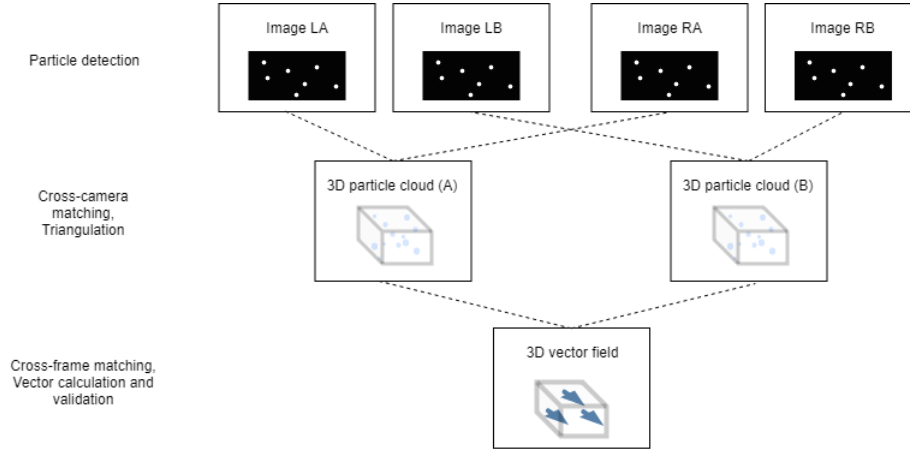


Figure 9: Data processing flowchart

5 Data processing

The purpose of 3DPTV data processing is to calculate the velocity field within the measurement domain from the captured images. There are 2 main strategies we can outline. First, is reconstructing the 3D distribution of particles prior to cross-frame matching (tracking). The order is reversed in the second strategy with 2D vectors calculated from the images and then matched to calculate the 3D velocities. As noted by Ouellette et al. [169], the first method is preferable, since then cross-frame matching is performed on a less dense, non-overlapping, 3D set of particles. The main steps of 3DPTV data processing are presented in Figure 9. All the code was implemented in MATLAB. The code is vectorized and/or parallelized where possible for best performance. In this section, we will discuss our approach to each of the steps.

5.1 Particle center localization

After a batch of images is input, image processing takes place. This includes masking, background subtraction, binarization, particle detection and particle center localization. The code is capable of dealing with multiple partially-overlapping particles by representing the cluster as a sum of Gaussians and recovering the subpixel positions of all the peaks [169]. Since the Hele-Shaw chip we are using here is shallow, we may afford higher seeding densities with the overlapping causing less problems. The centers of standalone particles are found using a quick and accurate symmetry-based localization algorithm [170], [171]. The symmetry algorithm typically works better for smaller particle images (diameter < 15px), like as the ones encountered during the experiment. For large images, such as the ones of the calibration dots, the symmetry is often lost which is why using a simple centroid calculation in that case gives better results. A good review and comparison of center-finding algorithms can be found in [172], [173], [169].

5.2 Cross-camera particle matching

After the particle centers have been detected in all the loaded images, we need to find point correspondences between the cameras. This is a well-known problem typically solved using epipolar constraints [99]. Due to the fact that our images are taken through a refractive interface, we offer a slightly different approach which naturally fits into the framework we have

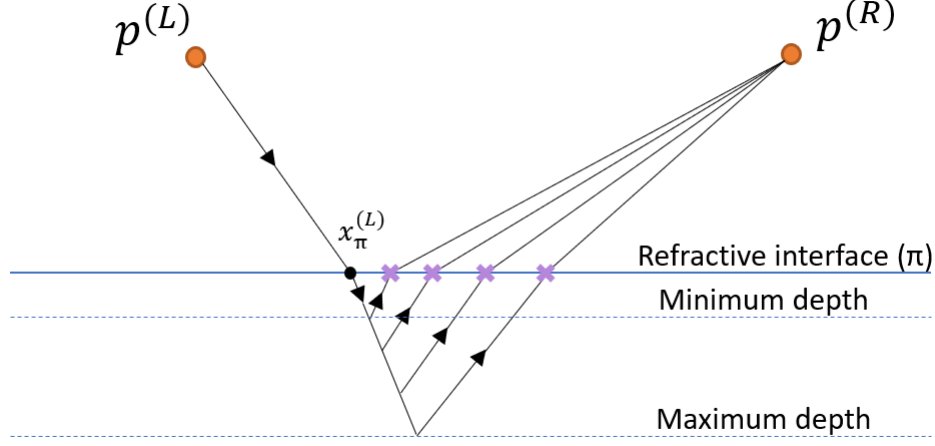


Figure 10: Cross-camera matching.

developed up to this point. The process is shown in 2D in Figure 10. For each detected particle i in the left image, we first back-project it onto the chip surface using $I_\pi^{(L)-1}$. Knowing the location of the projection center of the left camera $\mathbf{p}^{(L)}$, from it, we can reconstruct the left-view ray to the back-projected particle image on the chip surface ($x_{\pi i}^{(L)}$). Next, we calculate the refracted ray using the Snell's law and choose a few (at least 3) locations on it. Let us define a function:

$$W_\pi(\mathbf{x}_\pi^{(k)}, \mathbf{x}_w; \mathbf{p}^{(k)}, \pi, n_{ref}) = 0 \quad (13)$$

where $\mathbf{x}_{\pi i}^{(k)}$ is, as defined previously, the π -plane trace of the refracted ray directed from the center of projection of the camera $\mathbf{p}^{(k)}$ to the point \mathbf{x}_w . The function W_π is implicit and is solved numerically. We assume that the

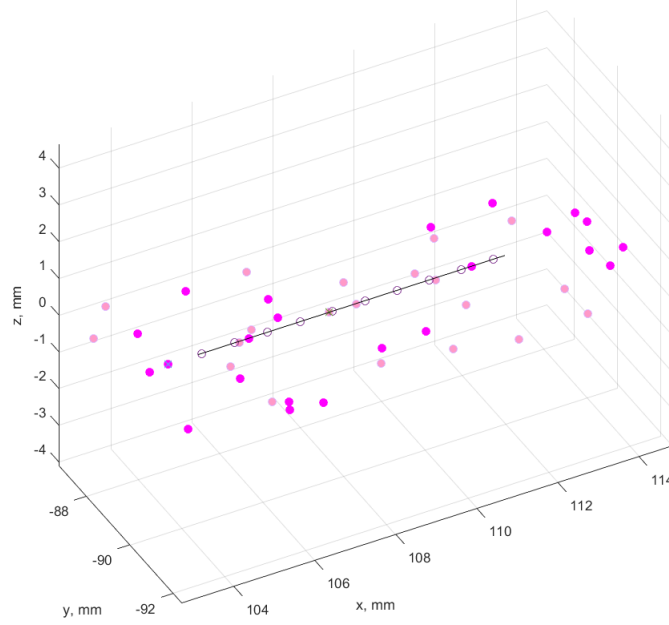


Figure 11: Quadratic curve, marking the locus of potential matching particles. Dark pink dots denote left camera ray traces and light pink - right-camera traces on the π plane.

refractive index n_{ref} and the orientation and the position of the plane π are given. From the chosen locations (\mathbf{x}_w), solving W_π , we find the points where the reconstructed right-view ray intersects the refractive interface marked with crosses in Figure 10. We fit a quadratic curve Q_i to the found points (Figure 11). Note that we consider only a feasible segment of the curve starting from the surface point corresponding to the minimum depth and ending with the one corresponding to the maximum depth. Next, we back-project the particle images from the right camera onto the plane π to obtain $\{\mathbf{x}_{\pi j}^{(R)}\}_{j=1}^N$ (light pink in Figure 11) out of which we find those closest to the

curve Q_i , using Delaunay triangulation, and calculate the distance (c_{ij}) for such points using the Cardano's formula. Potential matches are identified by setting a maximum distance threshold. Here i and j are the indices of the particle in the left camera image and its potential match particle in the right camera respectively. An $M \times N$ cost matrix C is built where M and N are the numbers of particles in the left and right images. Each entry of matrix C is populated by the available c_{ij} . The rest of the matrix is set to infinity as impossible solutions. We have thus formulated the cross-camera matching problem as a well-known general assignment problem. Hungarian algorithm is used to find a globally optimal solution [174], [169], [175]. A similar approach can be found in [117].

5.3 3D reconstruction of particle positions

3D reconstruction of the particle cloud is performed by triangulation from the two recorded views. Conventionally, this task is also handled by epipolar geometry, however some adjustments must be implemented to take the refractive interface into account which will be discussed here. The process of triangulation comprises finding a 3D position of a physical point by reconstructing the principal light rays which produced the recorded images [176], [177]. In reality, the challenge of triangulation is the fact that due to the noise in the recorded signal, the reconstructed rays, in general, will not intersect at a single point in space. One of the simplest ways to estimate the position of the physical point is taking it to be the midpoint between the

crossing lines lying on their mutual perpendicular. A better estimate can be obtained if we generalize this approach by instead weighing the distance from each ray along the perpendicular by a function of the distance from the respective cameras (projection centers). If the image noise is assumed Gaussian, an optimal triangulation can be obtained by minimizing the total amount by which the images need to be corrected in order to converge at the point [178], [179]. While a closed-form solution can be derived for the case of measurements in air or some other homogeneous environment, the presence of the refractive interface complicates the model. Using the obtained empirical calibration polynomials, we solve the triangulation problem by minimizing the following function:

$$\epsilon_t(\mathbf{x}_w) = \|\mathbf{X}^{(L)} - I_\pi^{(L)}(W_\pi(\mathbf{x}_w, \mathbf{p}^{(L)}))\|^2 + \|\mathbf{X}^{(R)} - I_\pi^{(R)}(W_\pi(\mathbf{x}_w, \mathbf{p}^{(R)}))\|^2 \quad (14)$$

The initial guess for \mathbf{x}_w is supplied by the weighted midpoint method described above.

5.4 Cross-frame particle matching

At this point, we have two snapshots of the particle cloud separated by the known Δt . While a lot of particle tracking techniques rely on time-series information [169], [40], [38], here we employ 2-frame tracking which is a good fit for the straddle imaging pattern described in the section 4. Possibly the simplest 2-frame matching algorithm would be nearest-neighbor matching where

the particles in frame A are matched to their nearest neighbors in frame B. This approach can work only at low tracking densities defined as a ratio of the mean interframe displacement to mean distance between the particles. A good review of 2-frame tracking techniques can be found in [180]. Here we employ the classical relaxation algorithm [181], [168] which iteratively updates the chance of match based on the behavior of the neighbor particles. Relaxation method has been shown to perform well under high gradients [180] and high seeding densities [95]. There are several minor modifications to the method we have implemented for our experiment. First, we use boxes and not spheres to define neighbors and potential matches around the particles. Boxes are a better choice for cases where the flow is more uniformly directed. Second, the search volumes for the matches vary by particle and expand non-uniformly until enough number of neighbors or potential matches is found. The exact numbers are, of course, adjustable. For more uniformly-directed flows, expansion in one direction may be preferred to other, since we are looking for neighbor particles with similar motion. Expanding the neighbor search region in the direction of gradient will lead to poor results. Finally, specifically for the application in fractures, we use a variable height of the search boxes, proportional to the local aperture of the fracture model. This improves the quality of the velocity data, since finer measurements are needed to resolve high velocity gradients at small-aperture locations. The downside of the relaxation method is that it is iterative and thus is more computationally-demanding and time-consuming than some other alterna-

tives. Non-iterative schemes which can approach the accuracy of the relaxation algorithm have been offered in the literature [95].

5.5 Vector calculation and validation

In two-frame tracking methods as the one presented here, the calculation of vectors after the cross-frame matching is straightforward. Having the position of the particle in timeframes A ($\mathbf{x}_w^{(A)}$) and B ($\mathbf{x}_w^{(B)}$), we calculate the velocity vector as:

$$\mathbf{v} = \mathbf{x}_w^{(B)} - \mathbf{x}_w^{(A)}$$

Vector validation is performed based on the neighbors. The challenge for PTV data is that it is not structured as is PIV data. We have implemented the popular method developed by Duncan et al. [182] for unstructured velocity fields, based on normalized residuals. The neighboring vectors are found using Delaunay triangulation. Given a vector in question \mathbf{v} , and a set of its neighbor vectors v_i located at distances d_i , the normalized residual is calculated as:

$$r = \frac{\left| \frac{v}{\text{med}(d_i) + \epsilon_a} - \text{med} \left(\frac{v_i}{d_i + \epsilon_a} \right) \right|}{\text{med} \left| \frac{v_i}{d_i + \epsilon_a} - \text{med} \left(\frac{v_i}{d_i + \epsilon_a} \right) \right| + \epsilon_a}$$

where ϵ_a is an adjustable threshold. We use a user-feedback loop to adjust the threshold for the residuals interactively plotting the preview results.

Parameter	Camera 1	Camera 2
r_1	3.22E-05	3.21E-05
r_2	-1.26E-08	-1.43E-08
p_1	1.41E-05	-2.43E-05
p_2	7.24E-07	-1.33E-05
q_1	0.107	0.096
q_2	0.009	-0.004
q_3	-0.994	0.995
q_4	-0.004	-0.001
t_x, mm	65.304	83.069
t_y, mm	53.307	55.240
t_z, mm	235.492	268.058
$\rho, ^\circ$	120.550	251.586
$\tau, ^\circ$	2.578	2.9221
f_v, mm	-51.532	-51.744
s_X, mm	5.50E-03	5.50E-03
s_Y, mm	5.50E-03	5.50E-03
c_{dx}, px	3213.096	3501.131
c_{dy}, px	2197.704	2232.534

Table 1: Calibration parameters.

6 Results

6.1 Calibration results

In the Table 1 the results of the calibration are shown. From the vector \mathbf{t} , we calculated the position of the cameras (Equation 12) to be:

$$p^{(L)} = [14.64 \quad -54.34 \quad 243.7]^T$$

$$p^{(R)} = [133.14 \quad -54.11 \quad 247.29]^T$$

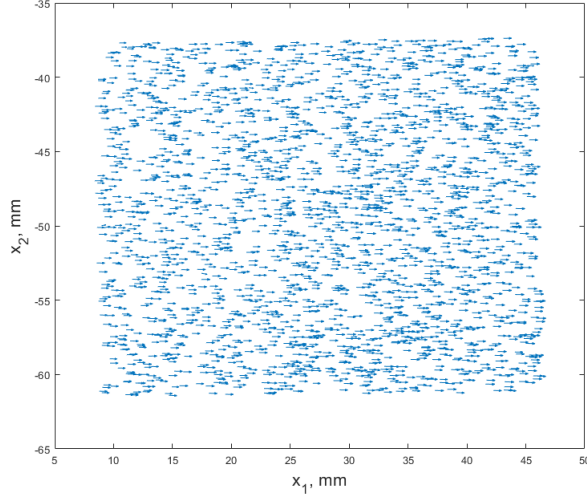


Figure 12: Vectors, connecting the π -plane traces of the rays from the particles, matched across cameras.

respectively. We can see how the regressed values of the tilt angles are close to the actual values, set on the camera objectives. Interestingly, the values of ρ have consistently been different by about 20-30 degrees from the expected values. The rest of the parameters are allowed to vary freely within acceptable bounds and attain reasonable values within the expected ranges. We confirm that distortion center is shifted from the center of the image in the expected direction by a value correlated with lens tilt.

6.2 Experimental results

The results shown here are for only two consecutive frames. We have found that by tuning parameters of Gaussian fitting algorithm, we are able to recover individual positions from clusters of 10+ particles. This improves the

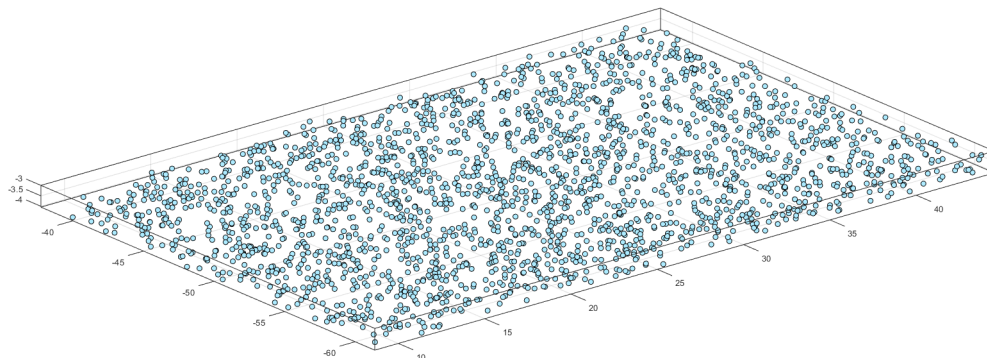


Figure 13: 3D reconstruction of the particle cloud in Frame A.

yield of the technique and data density. Figure 12 shows the result of such matching. Those are not velocity vectors yet, those are vectors connecting the π -plane traces ($x_{\pi}^{(L)}$ and $x_{\pi}^{(R)}$) of rays emanating from the particles matched across the cameras. We can see that all the vectors are parallel and are approximately equal in length. This shows the internal consistency of the particle matches. Next, we calculate the 3D particle distribution in the two timeframes. Figure 13 shows such a reconstructed particle cloud at frame A viewed from the side (in y -direction). Note, how the parallel walls of the model can clearly be discerned from the cloud. We can calculate the thickness of the model to be approximately 800 microns as expected. Also, a tilt in the particle cloud can be seen. This tilt is only about 0.5 degrees and it can be attributed to the imperfections in manufacturing of the chip, possibly, due to a not perfectly level position of the mold in which the chip parts were cast. From the two snapshots, the velocity field in the Hele-Shaw model was calculated. The displacement distribution in the xy plane (top view) is shown

in Figure 14. Note, how all the vectors are unidirectional but are of different magnitude due to different depths. Also note, how the displacement vectors tend to slightly curve at the bottom edge of the measurement window. This is due to the fact that an air bubble was present just outside the measurement window during the experiment. Finally, Figure 15 shows the side view of the model, v_x v.s. z . We can see how the displacements follow a parabolic profile, as expected, peaking at $0.28mm$. From the graph, we once again confirm the expected height of the flow chamber of the chip. The errors, recorded for the in-plane and out-of-plane position components are 1.5 and 11.5 microns respectively. As expected, the out-of-plane component of the position is larger than the in-plane counterparts. We explore and compare the errors in our numerical error study of sensitivity of error in calculating physical position to the error of finding image position. Note that the data presented here was extracted from only two frames. A much better-quality picture can be obtained if the steady-state nature of the flow is exploited and the velocity data is averaged over the course of the experiment.

6.3 Error analysis

In this subsection, we are going to calculate the expected maximum displacement and compare it to the measured maximum displacement of $0.28mm/s$. Let q be the injection flow rate, W and H - respectively, the width and the

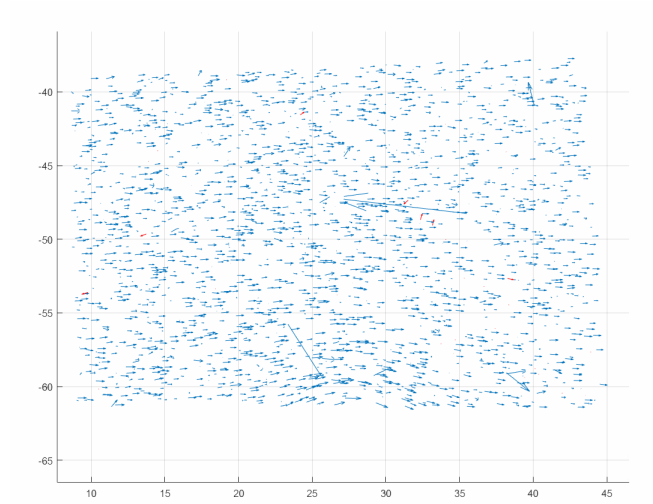


Figure 14: Raw, measured velocity field, top view. Curved motion due to a bubble can be noticed at the bottom of the FOV.

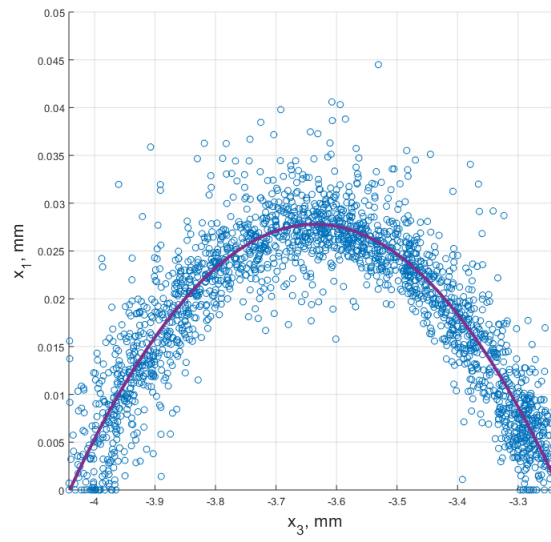


Figure 15: Raw, measured velocity field, side view, fit with a parabola.

height of the flow chamber, then the maximum displacement is calculated as:

$$dx_{max} = \frac{3}{2} \frac{q}{WH} \Delta t$$

Then, the corresponding error of dx_{max} is:

$$\sigma_{dx_{max}} = \sqrt{\left(\frac{\sigma_q}{q}\right)^2 + \left(\frac{\sigma_{\Delta t}}{\Delta t}\right)^2 + \left(\frac{\sigma_W}{W}\right)^2 + \left(\frac{\sigma_H}{H}\right)^2} \quad (15)$$

$\sigma_{\Delta t}$ and σ_q are negligible. We use a ruler measurement error for $\sigma_W \approx \sqrt{2} \text{ mm}$, and manufacturing tolerance for $\sigma_W \approx 0.04 \text{ mm}$. Then equation 15 gives $\sigma_{dx_{max}} = 0.053$, leading to a 0.026 ± 0.003 95% confidence interval for the expected maximum displacement. We can see how our measured maximum displacement falls between the bounds. More insight into the accuracy of the system can be found in Appendix B.

7 Summary

In this report, we have reviewed a variety of measurement techniques capable of delivering 3D3C velocity data. We explained the challenge of velocimetry and imaging, in general, when a refractive interface is present and covered the efforts which have been reported so far to address this issue. We offered a detailed description of our 3DPTV setup which handles the refractive interface in a novel way and relies on the state-of-the art models and algorithms. The problem of possible unknown refractive surface geometry (such as in natural

fractures) is solved by using a working fluid with a matched refractive index. The software for calibration and data processing has been implemented in the MATLAB IDE. Finally, preliminary validation results have been presented. The measured velocity profile is within the expected range, however a more accurate test with stricter confidence bounds needs to be performed to further validate the system. The presented results are extracted from only two frames. A significant improvement in the measurement quality is expected if velocity results are averaged across multiple frames, as is permissible with a steady-state flow.

8 Practical notes

1. To avoid bubbles, the model should be filled at a tilt. The outlet section should be higher than the inlet, so that the bubbles rise and exit through the outlet port. Slight tapping of the model in the area of the stuck bubbles may help mobilize the bubbles.

2. During the experiment, probably due to the rise of temperature, bubbles will start appearing in the model. These bubbles are especially prevalent at the light-receiving edge of the model which leads to think that in fact the temperature change is indeed to blame, since that side is heated up by the laser most. These bubbles act like opaque obstructions to light and produce dark shadows in the model (Krug et al. [77] faced a similar problem. The light simply does not reach those areas to trigger fluorescence. While the ve-

locity information in those areas is lost, using Fourier filtering, as suggested by Munch et al [183], can help recover the LIF information. The most effective way to reduce the appearance of the bubbles with additional investment is circulating the liquid as much as possible especially during the periods of laser illumination.

3. We can reduce the number of variables when focusing a tilt-shift camera in our experiment. Use the objective focus ring to bring the middle of the desired plane in focus while the FOV is centered around the chip. Then, start adjusting the tilt of the lens to bring the entire desired plane into focus. In this position, the lens tilt rotates the focal plane approximately around the midpoint of the FOV.

9 Recommendations

Here are some points which could be implemented to further improve the quality of the data produced by the 3DPTV system.

1. Implement more advanced denoising techniques such as non-local means to improve the image quality.
2. Try the dual-plane camera model for potential accuracy improvements.
3. Use vector validation to improve the validity of particle matching.
4. Implement non-iterative particle matching algorithms.
5. Adjust the camera sensor tilt angles.

References

- [1] D. Cardano, G. Carlino, and A. Cogotti, “Piv in the car industry: State-of-the-art and future perspectives”, in *Particle Image Velocimetry: New Developments and Recent Applications*. Berlin, Heidelberg: Springer Berlin Heidelberg, 2008, pp. 363–376. DOI: 10.1007/978-3-540-73528-1_19. [Online]. Available: https://doi.org/10.1007/978-3-540-73528-1_19.
- [2] E. Lobutova, C. Resagk, and T. Putze, “Investigation of large-scale circulations in room air flows using three-dimensional particle tracking velocimetry”, *Building and Environment*, vol. 45, no. 7, pp. 1653–1662, 2010.
- [3] D. J. Garmann, M. R. Visbal, and P. D. Orkwis, “Three-dimensional flow structure and aerodynamic loading on a revolving wing”, *Physics of Fluids*, vol. 25, no. 3, p. 034101, 2013. DOI: 10.1063/1.4794753. eprint: <https://doi.org/10.1063/1.4794753>. [Online]. Available: <https://doi.org/10.1063/1.4794753>.
- [4] D. Prohasky, R. Moya Castro, S. Watkins, and J. Burry, “Design driven physical experimentation: A flexible wind sensing platform for architects”, in *CAADRIA 2016: Living Systems and Micro-Utopias: Towards Continuous Designing*, Association for Computer-Aided Architectural Design Research in Asia, 2016, pp. 239–248.
- [5] J. K. Kim, J.-H. Yoon, C. H. Kim, T. W. Nam, D. B. Shim, and H. A. Shin, “Particle image velocimetry measurements for the study of nasal airflow”, *Acta Oto-Laryngologica*, vol. 126, no. 3, pp. 282–287, 2006. DOI: 10.1080/00016480500361320. eprint: <https://doi.org/10.1080/00016480500361320>. [Online]. Available: <https://doi.org/10.1080/00016480500361320>.
- [6] V. A. Troutman and J. O. Dabiri, “Single-camera three-dimensional tracking of natural particulate and zooplankton”, *Measurement Science and Technology*, vol. 29, no. 7, p. 075401, 2018.
- [7] J. Martin, “Go fast with the flow”, *Mechanical Engineering Magazine Select Articles*, vol. 137, no. 05, pp. 40–45, 2015.

- [8] J. Martin, P. Oshkai, and N. Djilali, “Flow structures in a u-shaped fuel cell flow channel: Quantitative visualization using particle image velocimetry”, *Journal of Fuel Cell Science and Technology - J FUEL CELL SCI TECHNOL*, vol. 2, Feb. 2005. DOI: 10.1115/1.1843121.
- [9] W. P. D. Ehrfeld, K. D. Golbig, V. Hessel, H. R. Lo, and T. Richter, “Characterization of mixing in micromixers by a test reaction: Single mixing units and mixer arrays”, 1999.
- [10] M. Oishi, H. Kinoshita, T. Fujii, and M. Oshima, “Simultaneous measurement of internal and surrounding flows of a moving droplet using multicolour confocal micro-particle image velocimetry (micro-PIV)”, *Measurement Science and Technology*, vol. 22, no. 10, p. 105 401, Aug. 2011. DOI: 10.1088/0957-0233/22/10/105401. [Online]. Available: <https://doi.org/10.1088%2F0957-0233%2F22%2F10%2F105401>.
- [11] H. Kinoshita, S. Kaneda, T. Fujii, and M. Oshima, “Three-dimensional measurement and visualization of internal flow of a moving droplet using confocal micro-piv”, *Lab Chip*, vol. 7, pp. 338–346, 3 2007. DOI: 10.1039/B617391H. [Online]. Available: <http://dx.doi.org/10.1039/B617391H>.
- [12] M. Heshmati and M. Piri, “Interfacial boundary conditions and residual trapping: A pore-scale investigation of the effects of wetting phase flow rate and viscosity using micro-particle image velocimetry”, *Fuel*, vol. 224, pp. 560–578, 2018, ISSN: 0016-2361. DOI: <https://doi.org/10.1016/j.fuel.2018.03.010>. [Online]. Available: <http://www.sciencedirect.com/science/article/pii/S0016236118303971>.
- [13] F. Kazemifar, G. Blois, D. C. Kyritsis, and K. T. Christensen, “A methodology for velocity field measurement in multiphase high-pressure flow of co2 and water in micromodels”, *Water Resources Research*, vol. 51, no. 4, pp. 3017–3029, 2015. DOI: 10.1002/2014WR016787. eprint: <https://agupubs.onlinelibrary.wiley.com/doi/pdf/10.1002/2014WR016787>. [Online]. Available: <https://agupubs.onlinelibrary.wiley.com/doi/abs/10.1002/2014WR016787>.
- [14] F. Menna, F. Remondino, and H.-G. Maas, *Sensors and Techniques for 3D Object Modeling in Underwater Environments*. Switzerland: Mdpi AG, 2016, ISBN: 3038422223, 9783038422228.

- [15] Y. Qian, Y. Zheng, M. Gong, and Y.-H. Yang, “Simultaneous 3d reconstruction for water surface and underwater scene”, in *ECCV*, 2018.
- [16] Y.-S. Wu, “Chapter 9 - multiphase flow in fractured porous media”, in *Multiphase Fluid Flow in Porous and Fractured Reservoirs*, Y.-S. Wu, Ed., Boston: Gulf Professional Publishing, 2016, pp. 207–250, ISBN: 978-0-12-803848-2. DOI: <https://doi.org/10.1016/B978-0-12-803848-2.00009-X>. [Online]. Available: <http://www.sciencedirect.com/science/article/pii/B978012803848200009X>.
- [17] M. Arshadi, M. Khishvand, A. Aghaei, M. Piri, and G. A. Al-Muntasheri, “Pore-scale experimental investigation of two-phase flow through fractured porous media”, *Water Resources Research*, vol. 54, no. 5, pp. 3602–3631, 2018. DOI: 10.1029/2018WR022540. eprint: <https://agupubs.onlinelibrary.wiley.com/doi/pdf/10.1029/2018WR022540>. [Online]. Available: <https://agupubs.onlinelibrary.wiley.com/doi/abs/10.1029/2018WR022540>.
- [18] A. M. Saidi, *Reservoir Engineering of Fractured Reservoirs (fundamental and Practical Aspects)*. Total, 1987.
- [19] R. L. Detwiler, H. Rajaram, and R. J. Glass, “Solute transport in variable-aperture fractures: An investigation of the relative importance of taylor dispersion and macrodispersion”, *Water Resources Research*, vol. 36, no. 7, pp. 1611–1625, 2000. DOI: 10.1029/2000WR900036. eprint: <https://agupubs.onlinelibrary.wiley.com/doi/pdf/10.1029/2000WR900036>. [Online]. Available: <https://agupubs.onlinelibrary.wiley.com/doi/abs/10.1029/2000WR900036>.
- [20] T. Fuchs, R. Hain, and C. J. Kähler, “Uncertainty quantification of three-dimensional velocimetry techniques for small measurement depths”, *Experiments in Fluids*, vol. 57, no. 5, p. 73, Apr. 2016, ISSN: 1432-1114. DOI: 10.1007/s00348-016-2161-5. [Online]. Available: <https://doi.org/10.1007/s00348-016-2161-5>.
- [21] M. Kegalj and H.-P. Schiffer, “Endoscopic piv measurements in a low pressure turbine rig”, *Experiments in Fluids*, vol. 47, no. 4, p. 689, Jul. 2009, ISSN: 1432-1114. DOI: 10.1007/s00348-009-0712-8. [Online]. Available: <https://doi.org/10.1007/s00348-009-0712-8>.

- [22] C. Poelma, “Ultrasound imaging velocimetry: A review”, *Experiments in Fluids*, vol. 58, no. 1, p. 3, Dec. 2016, ISSN: 1432-1114. DOI: 10.1007/s00348-016-2283-9. [Online]. Available: <https://doi.org/10.1007/s00348-016-2283-9>.
- [23] W.-K. Lee, K. Fezzaa, and T. Uemura, “Three-dimensional x-ray micro-velocimetry”, *Journal of synchrotron radiation*, vol. 18, no. 2, pp. 302–304, 2011.
- [24] F. Alberini, L. Liu, E. Stitt, and M. Simmons, “Comparison between 3-d-ptv and 2-d-piv for determination of hydrodynamics of complex fluids in a stirred vessel”, *Chemical Engineering Science*, vol. 171, pp. 189–203, 2017.
- [25] S. Fu, P. H. Biwale, and C. Mathis, “Numerical and experimental comparison of 3d particle tracking velocimetry (ptv) and particle image velocimetry (piv) accuracy for indoor airflow study”, *Building and Environment*, vol. 100, pp. 40–49, 2016.
- [26] S. Hagsäter, C. Westergaard, H. Bruus, and J. P. Kutter, “A compact viewing configuration for stereoscopic micro-piv utilizing mm-sized mirrors”, *Experiments in fluids*, vol. 45, no. 6, p. 1015, 2008.
- [27] J. Estevadeordal and L. Goss, “Piv with led: Particle shadow velocimetry (psv) technique”, in *43rd AIAA aerospace sciences meeting and exhibit*, 2005, p. 37.
- [28] M. BORN and E. WOLF, “Chapter xiii - optics of metals”, in *Principles of Optics (Sixth Edition)*, M. BORN and E. WOLF, Eds., Sixth Edition, Pergamon, 1980, pp. 611–664, ISBN: 978-0-08-026482-0. DOI: <https://doi.org/10.1016/B978-0-08-026482-0.50020-7>. [Online]. Available: <http://www.sciencedirect.com/science/article/pii/B9780080264820500207>.
- [29] Thermo Fischer Scientific, “Fluorescence spectraviewer”, [Online]. Available: <https://www.thermofisher.com/us/en/home/life-science/cell-analysis/labeling-chemistry/fluorescence-spectraviewer.html>.
- [30] J. R. Lakowicz, “Effects of solvents on fluorescence emission spectra”, in *Principles of Fluorescence Spectroscopy*. Boston, MA: Springer US, 1983, pp. 187–215, ISBN: 978-1-4615-7658-7. DOI: 10.1007/978-1-

4615-7658-7_7. [Online]. Available: https://doi.org/10.1007/978-1-4615-7658-7_7.

- [31] R. Lindken, M. Rossi, S. Große, and J. Westerweel, “Micro-particle image velocimetry (μpiv): Recent developments, applications, and guidelines”, *Lab on a Chip*, vol. 9, no. 17, pp. 2551–2567, 2009.
- [32] J. M. Martel and M. Toner, “Inertial focusing in microfluidics”, *Annual review of biomedical engineering*, vol. 16, pp. 371–396, 2014.
- [33] P. Saffman, “The lift on a small sphere in a slow shear flow”, *Journal of fluid mechanics*, vol. 22, no. 2, pp. 385–400, 1965.
- [34] X. Zheng and Z. Silber-Li, “The influence of saffman lift force on nanoparticle concentration distribution near a wall”, *Applied physics letters*, vol. 95, no. 12, p. 124 105, 2009.
- [35] R. Mei, “Velocity fidelity of flow tracer particles”, *Experiments in Fluids*, vol. 22, no. 1, pp. 1–13, 1996.
- [36] A. Melling, “Tracer particles and seeding for particle image velocimetry”, *Measurement Science and Technology*, vol. 8, no. 12, p. 1406, 1997.
- [37] J. G. Santiago, S. T. Wereley, C. D. Meinhart, D. Beebe, and R. J. Adrian, “A particle image velocimetry system for microfluidics”, *Experiments in fluids*, vol. 25, no. 4, pp. 316–319, 1998.
- [38] M. Raffel, C. E. Willert, F. Scarano, C. J. Kähler, S. T. Wereley, and J. Kompenhans, *Particle image velocimetry: a practical guide*. Springer, 2018.
- [39] R. J. Adrian and J. Westerweel, *Particle image velocimetry*, 30. Cambridge University Press, 2011.
- [40] C. Cierpka, B. Lütke, and C. J. Kähler, “Higher order multi-frame particle tracking velocimetry”, *Experiments in Fluids*, vol. 54, no. 5, p. 1533, 2013.
- [41] Y. A. Hassan and R. E. Canaan, “Full-field bubbly flow velocity measurements using a multiframe particle tracking technique”, *Experiments in Fluids*, vol. 12, no. 1, pp. 49–60, Dec. 1991, ISSN: 1432-1114. DOI: 10.1007/BF00226565. [Online]. Available: <https://doi.org/10.1007/BF00226565>.

- [42] J. Xiong, R. Idoughi, A. A. Aguirre-Pablo, A. B. Aljedaani, X. Dun, Q. Fu, S. T. Thoroddsen, and W. Heidrich, “Rainbow particle imaging velocimetry for dense 3d fluid velocity imaging”, *ACM Trans. Graph.*, vol. 36, no. 4, 36:1–36:14, Jul. 2017, ISSN: 0730-0301. DOI: 10.1145/3072959.3073662. [Online]. Available: <http://doi.acm.org/10.1145/3072959.3073662>.
- [43] P. T. Tokumaru and P. E. Dimotakis, “Image correlation velocimetry”, *Experiments in Fluids*, vol. 19, no. 1, pp. 1–15, May 1995, ISSN: 1432-1114. DOI: 10.1007/BF00192228. [Online]. Available: <https://doi.org/10.1007/BF00192228>.
- [44] C. J. Kähler, S. Scharnowski, and C. Cierpka, “On the resolution limit of digital particle image velocimetry”, *Experiments in Fluids*, vol. 52, no. 6, pp. 1629–1639, Jun. 2012, ISSN: 1432-1114. DOI: 10.1007/s00348-012-1280-x. [Online]. Available: <https://doi.org/10.1007/s00348-012-1280-x>.
- [45] —, “On the uncertainty of digital piv and ptv near walls”, *Experiments in Fluids*, vol. 52, no. 6, pp. 1641–1656, Jun. 2012, ISSN: 1432-1114. DOI: 10.1007/s00348-012-1307-3. [Online]. Available: <https://doi.org/10.1007/s00348-012-1307-3>.
- [46] C. Cierpka and C. J. Kähler, “Particle imaging techniques for volumetric three-component (3d3c) velocity measurements in microfluidics”, *Journal of Visualization*, vol. 15, no. 1, pp. 1–31, Feb. 2012, ISSN: 1875-8975. DOI: 10.1007/s12650-011-0107-9. [Online]. Available: <https://doi.org/10.1007/s12650-011-0107-9>.
- [47] F. Scarano, “Iterative image deformation methods in PIV”, *Measurement Science and Technology*, vol. 13, no. 1, R1–R19, Nov. 2001. DOI: 10.1088/0957-0233/13/1/201. [Online]. Available: <https://doi.org/10.1088/0957-0233/13/1/201>.
- [48] D. P. Hart, “Super-resolution piv by recursive local-correlation”, *Journal of Visualization*, vol. 3, no. 2, pp. 187–194, Jun. 2000, ISSN: 1875-8975. DOI: 10.1007/BF03182411. [Online]. Available: <https://doi.org/10.1007/BF03182411>.
- [49] R. D. Keane, R. J. Adrian, and Y. Zhang, “Super-resolution particle imaging velocimetry”, *Measurement Science and Technology*, vol. 6, no. 6, pp. 754–768, Jun. 1995. DOI: 10.1088/0957-0233/6/6/013.

- [Online]. Available: <https://doi.org/10.1088/0957-0233/2F6%2F6%2F013>.
- [50] R. Bastiaans, G. van der Plas, and R. Kieft, “The performance of a new ptv algorithm applied in super-resolution piv”, *Experiments in Fluids*, vol. 32, no. 3, pp. 346–356, Mar. 2002, ISSN: 1432-1114. DOI: 10.1007/s003480100363. [Online]. Available: <https://doi.org/10.1007/s003480100363>.
 - [51] A. Stitou and M. L. Riethmuller, *Measurement Science and Technology*, vol. 12, no. 9, pp. 1398–1403, Aug. 2001. DOI: 10.1088/0957-0233/12/9/304. [Online]. Available: <https://doi.org/10.1088/0957-0233/12/9/304>.
 - [52] T. Hori and J. Sakakibara, “High-speed scanning stereoscopic PIV for 3d vorticity measurement in liquids”, *Measurement Science and Technology*, vol. 15, no. 6, pp. 1067–1078, May 2004. DOI: 10.1088/0957-0233/15/6/005. [Online]. Available: <https://doi.org/10.1088/0957-0233/15/6/005>.
 - [53] R. Bolaños-Jiménez, M. Rossi, D. Fernandez Rivas, C. J. Kähler, and A. Marin, “Streaming flow by oscillating bubbles: Quantitative diagnostics via particle tracking velocimetry”, *Journal of Fluid Mechanics*, vol. 820, pp. 529–548, 2017. DOI: 10.1017/jfm.2017.229.
 - [54] G. Cowan and H. H. Fairchild, “Introduction to the issue”, *Journal of Social Issues*, vol. 53, no. 3, pp. 409–415, 1997. DOI: 10.1111/j.1540-4560.1997.tb02118.x. eprint: <https://spssi.onlinelibrary.wiley.com/doi/pdf/10.1111/j.1540-4560.1997.tb02118.x>. [Online]. Available: <https://spssi.onlinelibrary.wiley.com/doi/abs/10.1111/j.1540-4560.1997.tb02118.x>.
 - [55] R. Vennell and R. Beatson, “A divergence-free spatial interpolator for large sparse velocity data sets”, *Journal of Geophysical Research: Oceans*, vol. 114, no. C10, 2009. DOI: 10.1029/2008JC004973. eprint: <https://agupubs.onlinelibrary.wiley.com/doi/pdf/10.1029/2008JC004973>. [Online]. Available: <https://agupubs.onlinelibrary.wiley.com/doi/abs/10.1029/2008JC004973>.
 - [56] L. D. C. Casa and P. S. Krueger, “Radial basis function interpolation of unstructured, three-dimensional, volumetric particle tracking velocimetry data”, *Measurement Science and Technology*, vol. 24, no. 6,

- p. 065 304, May 2013. DOI: 10.1088/0957-0233/24/6/065304. [Online]. Available: <https://doi.org/10.1088/0957-0233/24/6/065304>.
- [57] W. H. Tien, D. Dabiri, and J. R. Hove, “Color-coded three-dimensional micro particle tracking velocimetry and application to micro accelerating micro-channel flow”, Apr. 2019.
 - [58] C. Cierpka and C. Kähler, “Cross-correlation or tracking-comparison and discussion”, in *16th international symposium on applications of laser techniques to fluid mechanics, Lisbon, July, 2012*, pp. 9–12.
 - [59] H. Nobach and E. Bodenschatz, “Limitations of accuracy in piv due to individual variations of particle image intensities”, *Experiments in Fluids*, vol. 47, no. 1, pp. 27–38, Jul. 2009, ISSN: 1432-1114. DOI: 10.1007/s00348-009-0627-4. [Online]. Available: <https://doi.org/10.1007/s00348-009-0627-4>.
 - [60] C. Cierpka, M. Rossi, R. Segura, F. Mastrangelo, and C. J. Kähler, “A comparative analysis of the uncertainty of astigmatism- μ ptv, stereo- μ piv, and μ piv”, *Experiments in Fluids*, vol. 52, no. 3, pp. 605–615, Mar. 2012, ISSN: 1432-1114. DOI: 10.1007/s00348-011-1075-5. [Online]. Available: <https://doi.org/10.1007/s00348-011-1075-5>.
 - [61] M. Rossi, R. Segura, C. Cierpka, and C. J. Kähler, “On the effect of particle image intensity and image preprocessing on the depth of correlation in micro-piv”, *Experiments in Fluids*, vol. 52, no. 4, pp. 1063–1075, Apr. 2012, ISSN: 1432-1114. DOI: 10.1007/s00348-011-1194-z. [Online]. Available: <https://doi.org/10.1007/s00348-011-1194-z>.
 - [62] M. Wu, J. W. Roberts, and M. Buckley, “Three-dimensional fluorescent particle tracking at micron-scale using a single camera”, *Experiments in Fluids*, vol. 38, no. 4, pp. 461–465, Apr. 2005, ISSN: 1432-1114. DOI: 10.1007/s00348-004-0925-9. [Online]. Available: <https://doi.org/10.1007/s00348-004-0925-9>.
 - [63] C. E. Willert and M. Gharib, “Three-dimensional particle imaging with a single camera”, *Experiments in Fluids*, vol. 12, no. 6, pp. 353–358, Apr. 1992, ISSN: 1432-1114. DOI: 10.1007/BF00193880. [Online]. Available: <https://doi.org/10.1007/BF00193880>.

- [64] F. Pereira, M. Gharib, D. Dabiri, and D. Modarress, “Defocusing digital particle image velocimetry: A 3-component 3-dimensional dpiv measurement technique. application to bubbly flows”, *Experiments in Fluids*, vol. 29, no. 1, S078–S084, Dec. 2000, ISSN: 1432-1114. DOI: 10.1007/s003480070010. [Online]. Available: <https://doi.org/10.1007/s003480070010>.
- [65] E. Castaño Graff, F. J. A. Pereira, and M. Gharib, “Defocusing digital particle image velocimetry: A volumetric dpiv technique for dual and single phase flows”, pp. 2008–1, Jan. 2008.
- [66] L. Kajitani and D. Dabiri, “A full three-dimensional characterization of defocusing digital particle image velocimetry”, vol. 16, no. 3, pp. 790–804, Feb. 2005. DOI: 10.1088/0957-0233/16/3/022. [Online]. Available: <https://doi.org/10.1088/0957-0233/16/3/022>.
- [67] W. H. Tien, P. Kartes, T. Yamasaki, and D. Dabiri, “A color-coded backlighting defocusing digital particle image velocimetry system”, *Experiments in Fluids*, vol. 44, pp. 1015–1026, Jun. 2008. DOI: 10.1007/s00348-007-0457-1.
- [68] R. Hain, C. J. Kähler, and R. Radespiel, “Principles of a volumetric velocity measurement technique based on optical aberrations”, in *Imaging Measurement Methods for Flow Analysis*, W. Nitsche and C. Dobriloff, Eds., Berlin, Heidelberg: Springer Berlin Heidelberg, 2009, pp. 1–10, ISBN: 978-3-642-01106-1.
- [69] H. Kao and A. Verkman, “Tracking of single fluorescent particles in three dimensions: use of cylindrical optics to encode particle position”, *Biophysical Journal*, vol. 67, pp. 1291–1300, Sep. 1994. DOI: 10.1016/S0006-3495(94)80601-0.
- [70] A. Kumar, C. Cierpka, S. J. Williams, C. J. Kähler, and S. T. Wereley, “3d3c velocimetry measurements of an electrothermal microvortex using wavefront deformation ptv and a single camera”, *Microfluidics and Nanofluidics*, vol. 10, no. 2, pp. 355–365, Feb. 2011, ISSN: 1613-4990. DOI: 10.1007/s10404-010-0674-4. [Online]. Available: <https://doi.org/10.1007/s10404-010-0674-4>.

- [71] T. Fuchs, R. Hain, and C. J. Kähler, “Macroscopic three-dimensional particle location using stereoscopic imaging and astigmatic aberrations”, *Opt. Lett.*, vol. 39, no. 24, pp. 6863–6866, Dec. 2014. DOI: 10.1364/OL.39.006863. [Online]. Available: <http://ol.osa.org/abstract.cfm?URI=ol-39-24-6863>.
- [72] M. Rossi and C. J. Kähler, “Optimization of astigmatic particle tracking velocimeters”, *Experiments in Fluids*, vol. 55, no. 9, p. 1809, Aug. 2014, ISSN: 1432-1114. DOI: 10.1007/s00348-014-1809-2. [Online]. Available: <https://doi.org/10.1007/s00348-014-1809-2>.
- [73] Q. Gao, H. Wang, and J. Wang, “A single camera volumetric particle image velocimetry and its application”, *Science China Technological Sciences*, vol. 55, no. 9, pp. 2501–2510, Sep. 2012. DOI: 10.1007/s11431-012-4921-7. [Online]. Available: <https://doi.org/10.1007/s11431-012-4921-7>.
- [74] R. G. Racca and J. M. Dewey, “A method for automatic particle tracking in a three-dimensional flow field”, *Experiments in Fluids*, vol. 6, no. 1, pp. 25–32, Jan. 1988, ISSN: 1432-1114. DOI: 10.1007/BF00226131. [Online]. Available: <https://doi.org/10.1007/BF00226131>.
- [75] K. Peterson, B. Regaard, S. Heinemann, and V. Sick, “Single-camera, three-dimensional particle tracking velocimetry”, *Opt. Express*, vol. 20, no. 8, pp. 9031–9037, Apr. 2012. DOI: 10.1364/OE.20.009031. [Online]. Available: <http://www.opticsexpress.org/abstract.cfm?URI=oe-20-8-9031>.
- [76] H.-G. Maas, T. Putze, and P. Westfeld, “Recent developments in 3d-ptv and tomo-piv”, in *Imaging Measurement Methods for Flow Analysis*, W. Nitsche and C. Dobriloff, Eds., Berlin, Heidelberg: Springer Berlin Heidelberg, 2009, pp. 53–62, ISBN: 978-3-642-01106-1.
- [77] D. Krug, M. Holzner, B. Lüthi, M. Wolf, A. Tsinober, and W. Kinzelbach, “A combined scanning PTV/LIF technique to simultaneously measure the full velocity gradient tensor and the 3d density field”, *Measurement Science and Technology*, vol. 25, no. 6, p. 065301, Apr. 2014. DOI: 10.1088/0957-0233/25/6/065301. [Online]. Available: <https://doi.org/10.1088/0957-0233/25/6/065301>.

- [78] A. Maekawa and J. Sakakibara, “Development of multiple-eye PIV using mirror array”, *Measurement Science and Technology*, vol. 29, no. 6, p. 064011, May 2018. DOI: 10.1088/1361-6501/aab9f7. [Online]. Available: <https://doi.org/10.1088/1361-6501/aab9f7>.
- [79] K. D. Hinsch, “Holographic particle image velocimetry”, *Measurement Science and Technology*, vol. 13, no. 7, R61–R72, Jun. 2002. DOI: 10.1088/0957-0233/13/7/201. [Online]. Available: <https://doi.org/10.1088/0957-0233/13/7/201>.
- [80] T. W. Fahringer, K. P. Lynch, and B. S. Thurow, “Volumetric particle image velocimetry with a single plenoptic camera”, *Measurement Science and Technology*, vol. 26, no. 11, p. 115201, Sep. 2015. DOI: 10.1088/0957-0233/26/11/115201. [Online]. Available: <https://doi.org/10.1088/0957-0233/26/11/115201>.
- [81] C. Skupsch and C. Brücker, “Multiple-plane particle image velocimetry using a light-field camera”, *Opt. Express*, vol. 21, no. 2, pp. 1726–1740, Jan. 2013. DOI: 10.1364/OE.21.001726. [Online]. Available: <http://www.opticsexpress.org/abstract.cfm?URI=oe-21-2-1726>.
- [82] H. Chen and V. Sick, “Three-dimensional three-component air flow visualization in a steady-state engine flow bench using a plenoptic camera”, *SAE International Journal of Engines*, vol. 10, pp. 625–635, Mar. 2017. DOI: 10.4271/2017-01-0614.
- [83] C. Brücker, “Digital-particle-image-velocimetry (dpiv) in a scanning light-sheet: 3d starting flow around a short cylinder”, *Experiments in Fluids*, vol. 19, no. 4, pp. 255–263, Aug. 1995, ISSN: 1432-1114. DOI: 10.1007/BF00196474. [Online]. Available: <https://doi.org/10.1007/BF00196474>.
- [84] K. Hoyer, M. Holzner, B. Lüthi, M. Guala, A. Liberzon, and W. Kinzelbach, “3d scanning particle tracking velocimetry”, *Experiments in Fluids*, vol. 39, no. 5, p. 923, Aug. 2005, ISSN: 1432-1114. DOI: 10.1007/s00348-005-0031-7. [Online]. Available: <https://doi.org/10.1007/s00348-005-0031-7>.

- [85] T. J. McGregor, D. J. Spence, and D. W. Coutts, “Laser-based volumetric flow visualization by digital color imaging of a spectrally coded volume”, *Review of Scientific Instruments*, vol. 79, no. 1, p. 013 710, 2008. DOI: 10.1063/1.2825462. eprint: <https://doi.org/10.1063/1.2825462>. [Online]. Available: <https://doi.org/10.1063/1.2825462>.
- [86] A. A. Aguirre-Pablo, A. B. Aljedaani, J. Xiong, R. Idoughi, W. Heidrich, and S. T. Thoroddsen, “Single-camera 3d ptv using particle intensities and structured light”, *Experiments in Fluids*, vol. 60, no. 2, p. 25, Jan. 2019, ISSN: 1432-1114. DOI: 10.1007/s00348-018-2660-7. [Online]. Available: <https://doi.org/10.1007/s00348-018-2660-7>.
- [87] J. A. Mullin and W. J. A. Dahm, “Dual-plane stereo particle image velocimetry measurements of velocity gradient tensor fields in turbulent shear flow. i. accuracy assessments”, *Physics of Fluids*, vol. 18, no. 3, p. 035 101, 2006. DOI: 10.1063/1.2166447. eprint: <https://doi.org/10.1063/1.2166447>. [Online]. Available: <https://doi.org/10.1063/1.2166447>.
- [88] R. R. La Foy and P. Vlachos, “Multi-camera plenoptic particle image velocimetry”, 2013.
- [89] R. Lindken, J. Westerweel, and B. Wienieke, “Stereoscopic micro particle image velocimetry”, *Experiments in Fluids*, vol. 41, no. 2, pp. 161–171, Aug. 2006, ISSN: 1432-1114. DOI: 10.1007/s00348-006-0154-5. [Online]. Available: <https://doi.org/10.1007/s00348-006-0154-5>.
- [90] G. E. Elsinga, F. Scarano, B. Wienieke, and B. W. van Oudheusden, “Tomographic particle image velocimetry”, *Experiments in Fluids*, vol. 41, no. 6, pp. 933–947, Dec. 2006, ISSN: 1432-1114. DOI: 10.1007/s00348-006-0212-z. [Online]. Available: <https://doi.org/10.1007/s00348-006-0212-z>.
- [91] F. Scarano, “Tomographic PIV: principles and practice”, *Measurement Science and Technology*, vol. 24, no. 1, 012001, p. 012 001, Jan. 2013. DOI: 10.1088/0957-0233/24/1/012001.

- [92] A. Schröder, R. Geisler, K. Staack, G. E. Elsinga, F. Scarano, B. Wieneke, A. Henning, C. Poelma, and J. Westerweel, “Eulerian and Lagrangian views of a turbulent boundary layer flow using time-resolved tomographic PIV”, *Experiments in Fluids*, vol. 50, pp. 1071–1091, Apr. 2011. DOI: 10.1007/s00348-010-1014-x.
- [93] M. Novara and F. Scarano, “Performances of motion tracking enhanced tomo-piv on turbulent shear flows”, *Experiments in Fluids*, vol. 52, no. 4, pp. 1027–1041, Apr. 2012, ISSN: 1432-1114. DOI: 10.1007/s00348-011-1187-y. [Online]. Available: <https://doi.org/10.1007/s00348-011-1187-y>.
- [94] B. Wieneke, “Iterative reconstruction of volumetric particle distribution”, *Measurement Science and Technology*, vol. 24, no. 2, p. 024008, Dec. 2012. DOI: 10.1088/0957-0233/24/2/024008. [Online]. Available: <https://doi.org/10.1088/0957-0233/24/2/024008>.
- [95] T. Fuchs, R. Hain, and C. J. Kähler, “Non-iterative double-frame 2D/3D particle tracking velocimetry”, *Experiments in Fluids*, vol. 58, 119, p. 119, Sep. 2017. DOI: 10.1007/s00348-017-2404-0.
- [96] “The rate of dissipation of energy and the energy spectrum in a low-speed turbulent jet”, *Eos, Transactions American Geophysical Union*, vol. 37, no. 1, pp. 13–26, 1956. DOI: 10.1029/TR037i001p00013. eprint: <https://agupubs.onlinelibrary.wiley.com/doi/pdf/10.1029/TR037i001p00013>. [Online]. Available: <https://agupubs.onlinelibrary.wiley.com/doi/abs/10.1029/TR037i001p00013>.
- [97] K. Nishino, N. Kasagi, and M. Hirata, “Three-dimensional particle tracking velocimetry based on automated digital image processing”, *Journal of fluids engineering*, vol. 111, no. 4, pp. 384–391, 1989.
- [98] A. K. Prasad, “Stereoscopic particle image velocimetry”, *Experiments in Fluids*, vol. 29, no. 2, pp. 103–116, Aug. 2000. DOI: 10.1007/s003480000143. [Online]. Available: <https://doi.org/10.1007/s003480000143>.
- [99] H. G. Maas, A. Gruen, and D. Papantoniou, “Particle tracking velocimetry in three-dimensional flows”, *Experiments in Fluids*, vol. 15, no. 2, pp. 133–146, Jul. 1993, ISSN: 1432-1114. DOI: 10.1007/BF00190953. [Online]. Available: <https://doi.org/10.1007/BF00190953>.

- [100] N. A. Malik and T. Dracos, “Lagrangian ptv in 3d flows”, *Applied Scientific Research*, vol. 51, no. 1, pp. 161–166, Jun. 1993, ISSN: 1573-1987. DOI: 10.1007/BF01082531. [Online]. Available: <https://doi.org/10.1007/BF01082531>.
- [101] W. Brevis, Y. Niño, and G. H. Jirka, “Integrating cross-correlation and relaxation algorithms for particle tracking velocimetry”, *Experiments in Fluids*, vol. 50, no. 1, pp. 135–147, Jan. 2011, ISSN: 1432-1114. DOI: 10.1007/s00348-010-0907-z. [Online]. Available: <https://doi.org/10.1007/s00348-010-0907-z>.
- [102] H. Ha, K.-H. Nam, and S. J. Lee, “Hybrid piv-ptv technique for measuring blood flow in rat mesenteric vessels”, *Microvascular Research*, vol. 84, no. 3, pp. 242–248, 2012, ISSN: 0026-2862. DOI: <https://doi.org/10.1016/j.mvr.2012.07.004>. [Online]. Available: <http://www.sciencedirect.com/science/article/pii/S0026286212001264>.
- [103] X. Bao and M. Li, “Defocus and binocular vision based stereo particle pairing method for 3d particle tracking velocimetry”, *Optics and Lasers in Engineering*, vol. 49, no. 5, pp. 623–631, 2011, ISSN: 0143-8166. DOI: <https://doi.org/10.1016/j.optlaseng.2011.01.015>. [Online]. Available: <http://www.sciencedirect.com/science/article/pii/S0143816611000169>.
- [104] S. J. Lee and S. Kim, “Advanced particle-based velocimetry techniques for microscale flows”, *Microfluidics and Nanofluidics*, vol. 6, no. 5, p. 577, Jan. 2009, ISSN: 1613-4990. DOI: 10.1007/s10404-009-0409-6. [Online]. Available: <https://doi.org/10.1007/s10404-009-0409-6>.
- [105] C.-H. Yu, J.-H. Yoon, and H.-B. Kim, “Development and validation of stereoscopic micro-ptv using match probability”, *Journal of Mechanical Science and Technology*, vol. 23, no. 3, pp. 845–855, Mar. 2009, ISSN: 1976-3824. DOI: 10.1007/s12206-008-1209-8. [Online]. Available: <https://doi.org/10.1007/s12206-008-1209-8>.
- [106] D. Hirsch, E. C. Graff, F. Pereira, and M. Gharib, “Influence of common transparent materials on the accuracy of image-based velocimetry”, *Measurement Science and Technology*, vol. 26, no. 8, p. 087002, Jul. 2015. DOI: 10.1088/0957-0233/26/8/087002. [Online]. Available: <https://doi.org/10.1088/0957-0233/26/8/087002>.

- [107] D. C. Brown, “Close-range camera calibration”, *PHOTOGRAMMETRIC ENGINEERING*, vol. 37, no. 8, pp. 855–866, 1971.
- [108] R. Kotowski, J. Peipe, and W. Wester-Ebbinghaus, “Bundle triangulation in architectural photogrammetry: The basilica of san francesco in siena”, *The Photogrammetric Record*, vol. 12, no. 72, pp. 857–871, 1988. DOI: 10.1111/j.1477-9730.1988.tb00635.x. eprint: <https://onlinelibrary.wiley.com/doi/pdf/10.1111/j.1477-9730.1988.tb00635.x>. [Online]. Available: <https://onlinelibrary.wiley.com/doi/abs/10.1111/j.1477-9730.1988.tb00635.x>.
- [109] H. Klank, G. Goranovi, J. P. Kutter, H. Gjelstrup, J. Michelsen, and C. H. Westergaard, “PIV measurements in a microfluidic 3d-sheathing structure with three-dimensional flow behaviour”, *Journal of Micromechanics and Microengineering*, vol. 12, no. 6, pp. 862–869, Oct. 2002. DOI: 10.1088/0960-1317/12/6/318. [Online]. Available: <https://doi.org/10.1088/0960-1317/12/6/318>.
- [110] N. Moharana, “Three-dimensional lagrangian transport near the surface of a moving sphere”, English, Proefschrift., PhD thesis, Department of Applied Physics, Jun. 2016, ISBN: 978-90-386-4104-1.
- [111] J. Giardino, J. Hertzberg, and E. Bradley, “A calibration procedure for millimeter-scale stereomicroscopic particle image velocimetry”, *Experiments in Fluids*, vol. 45, no. 6, pp. 1037–1045, Dec. 2008, ISSN: 1432-1114. DOI: 10.1007/s00348-008-0525-1. [Online]. Available: <https://doi.org/10.1007/s00348-008-0525-1>.
- [112] J. G. Fryer and C. S. Fraser, “On the calibration of underwater cameras”, *The Photogrammetric Record*, vol. 12, no. 67, pp. 73–85, 1986. DOI: 10.1111/j.1477-9730.1986.tb00539.x. eprint: <https://onlinelibrary.wiley.com/doi/pdf/10.1111/j.1477-9730.1986.tb00539.x>. [Online]. Available: <https://onlinelibrary.wiley.com/doi/abs/10.1111/j.1477-9730.1986.tb00539.x>.
- [113] M. R. Shortis and J. W. Seager, “A practical target recognition system for close range photogrammetry”, *The Photogrammetric Record*, vol. 29, no. 147, pp. 337–355, 2014. DOI: 10.1111/phor.12070. eprint: <https://onlinelibrary.wiley.com/doi/pdf/10.1111/phor.12070>. [Online]. Available: <https://onlinelibrary.wiley.com/doi/abs/10.1111/phor.12070>.

- [114] C. Kunz and H. Singh, “Hemispherical refraction and camera calibration in underwater vision”, *OCEANS 2008*, pp. 1–7, 2008.
- [115] F. Menna, E. Nocerino, F. Fassi, and F. Remondino, “Geometric and optic characterization of a hemispherical dome port for underwater photogrammetry”, *Sensors*, vol. 16, no. 1, 2016, ISSN: 1424-8220. DOI: 10.3390/s16010048. [Online]. Available: <http://www.mdpi.com/1424-8220/16/1/48>.
- [116] W. H. Stevenson, H. D. Thompson, R. P. Durrett, and R. D. Gould, Eds., *A correction lens for Laser Doppler Velocimeter measurements in a cylindrical tube*, Jan. 1984.
- [117] S. B. Dalziel, “Decay of rotating turbulence: Some particle tracking experiments”, *Applied Scientific Research*, vol. 49, no. 3, pp. 217–244, Jul. 1992, ISSN: 1573-1987. DOI: 10.1007/BF00384624. [Online]. Available: <https://doi.org/10.1007/BF00384624>.
- [118] M. Moroni, N. Kleinfelter, and J. H. Cushman, “Analysis of dispersion in porous media via matched-index particle tracking velocimetry experiments”, *Advances in Water Resources*, vol. 30, no. 1, pp. 1–15, 2007, ISSN: 0309-1708. DOI: <https://doi.org/10.1016/j.advwatres.2006.02.005>. [Online]. Available: <http://www.sciencedirect.com/science/article/pii/S0309170806000388>.
- [119] D. Hill, D. Troolin, G. Walters, W. Lai, and K. Sharp, “Volumetric 3-component velocimetry (v3v) measurements of the turbulent flow in stirred tank reactors”, pp. 2008–1, Jan. 2008.
- [120] J. Kitzhofer and C. Brücker, “Tomographic particle tracking velocimetry using telecentric imaging”, *Experiments in Fluids*, vol. 49, no. 6, pp. 1307–1324, Dec. 2010, ISSN: 1432-1114. DOI: 10.1007/s00348-010-0879-z. [Online]. Available: <https://doi.org/10.1007/s00348-010-0879-z>.
- [121] M. Moroni and J. H. Cushman, “Statistical mechanics with three-dimensional particle tracking velocimetry experiments in the study of anomalous dispersion. ii. experiments”, *Physics of Fluids*, vol. 13, no. 1, pp. 81–91, 2001.
- [122] R. L. Stewart, I. D. Šutalo, and C. Y. Wong, “Three-dimensional tracking of sensor capsules mobilised by fluid flow”, *Measurement Science and Technology*, vol. 26, no. 3, p. 035302, 2015.

- [123] P. Westfeld and H.-G. Maas, “Photogrammetric techniques for voxel-based flow velocity field measurement”, *The Photogrammetric Record*, vol. 26, no. 136, pp. 422–438, 2011. DOI: 10.1111/j.1477-9730.2011.00656.x. eprint: <https://onlinelibrary.wiley.com/doi/pdf/10.1111/j.1477-9730.2011.00656.x>. [Online]. Available: <https://onlinelibrary.wiley.com/doi/abs/10.1111/j.1477-9730.2011.00656.x>.
- [124] M. D. Bethea, J. A. Lock, F. L. Merat, and P. Crouser, “Three-dimensional camera calibration technique for stereo imaging velocimetry experiments”, *Optical Engineering*, vol. 12, no. 136, pp. 3445–3454, 1997. DOI: 10.1117/1.601584. [Online]. Available: <https://doi.org/10.1117/1.601584>.
- [125] F. Pereira and M. Gharib, “Defocusing digital particle image velocimetry and the three-dimensional characterization of two-phase flows”, *Measurement Science and Technology*, vol. 13, no. 5, pp. 683–694, Mar. 2002. DOI: 10.1088/0957-0233/13/5/305. [Online]. Available: <https://doi.org/10.1088/0957-0233/13/5/305>.
- [126] M. Rossi, R. Lindken, and J. Westerweel, “Optimization of multi-plane μ piv for wall shear stress and wall topography characterization”, *Experiments in Fluids*, vol. 48, pp. 211–223, Feb. 2010. DOI: 10.1007/s00348-009-0725-3.
- [127] S. Y. Yoon, K. D. Kihm, and K. C. Kim, “Correlation of fluid refractive index with calibration coefficient for micro-defocusing digital particle image velocimetry”, *Measurement Science and Technology*, vol. 22, no. 3, p. 037001, Jan. 2011. DOI: 10.1088/0957-0233/22/3/037001. [Online]. Available: <https://doi.org/10.1088/0957-0233/22/3/037001>.
- [128] A. K. Prasad and K. Jensen, “Scheimpflug stereocamera for particle image velocimetry in liquid flows”, *Appl. Opt.*, vol. 34, no. 30, pp. 7092–7099, Oct. 1995. DOI: 10.1364/AO.34.007092. [Online]. Available: <http://ao.osa.org/abstract.cfm?URI=ao-34-30-7092>.
- [129] C. W. H. van Doorne and J. Westerweel, “Measurement of laminar, transitional and turbulent pipe flow using stereoscopic-piv”, *Experiments in Fluids*, vol. 42, no. 2, pp. 259–279, Feb. 2007, ISSN: 1432-

1114. DOI: 10.1007/s00348-006-0235-5. [Online]. Available: <https://doi.org/10.1007/s00348-006-0235-5>.
- [130] B. LÜTHI, A. TSINOBER, and W. KINZELBACH, “Lagrangian measurement of vorticity dynamics in turbulent flow”, *Journal of Fluid Mechanics*, vol. 528, pp. 87–118, 2005. DOI: 10.1017/S0022112004003283.
 - [131] U. Gülan, B. Lüthi, M. Holzner, A. Liberzon, A. Tsinober, and W. Kinzelbach, “Experimental study of aortic flow in the ascending aorta via particle tracking velocimetry”, *Experiments in Fluids*, vol. 53, Sep. 2012. DOI: 10.1007/s00348-012-1371-8.
 - [132] R. Kieft, K. Schreel, G. van der Plas, and C. Rindt, “The application of a 3d ptv algorithm to a mixed convection flow”, *Experiments in Fluids*, vol. 33, no. 4, pp. 603–611, Oct. 2002, ISSN: 1432-1114. DOI: 10.1007/s00348-002-0513-9. [Online]. Available: <https://doi.org/10.1007/s00348-002-0513-9>.
 - [133] V. Dore, M. Moroni, M. Le Menach, and A. Cenedese, “Investigation of penetrative convection in stratified fluids through 3d ptv”, *Experiments in Fluids*, vol. 47, pp. 811–825, Oct. 2009. DOI: 10.1007/s00348-009-0716-4.
 - [134] H. Kim, S. Große, G. E. Elsinga, and J. Westerweel, “Full 3d-3c velocity measurement inside a liquid immersion droplet”, *Experiments in Fluids*, vol. 51, no. 2, pp. 395–405, Aug. 2011, ISSN: 1432-1114. DOI: 10.1007/s00348-011-1053-y. [Online]. Available: <https://doi.org/10.1007/s00348-011-1053-y>.
 - [135] M. R. Bown, J. M. MacInnes, R. W. K. Allen, and W. B. J. Zimmerman, “Three-dimensional, three-component velocity measurements using stereoscopic micro-PIV and PTV”, *Measurement Science and Technology*, vol. 17, no. 8, pp. 2175–2185, Jul. 2006. DOI: 10.1088/0957-0233/17/8/017. [Online]. Available: <https://doi.org/10.1088/0957-0233/17/8/017>.
 - [136] J. Belden, “Calibration of multi-camera systems with refractive interfaces”, *Experiments in Fluids*, vol. 54, no. 2, p. 1463, Feb. 2013, ISSN: 1432-1114. DOI: 10.1007/s00348-013-1463-0. [Online]. Available: <https://doi.org/10.1007/s00348-013-1463-0>.

- [137] S. M. Soloff, R. J. Adrian, and Z.-C. Liu, “Distortion compensation for generalized stereoscopic particle image velocimetry”, *Measurement Science and Technology*, vol. 8, no. 12, pp. 1441–1454, Dec. 1997. DOI: 10.1088/0957-0233/8/12/008. [Online]. Available: <https://doi.org/10.1088/0957-0233/8/12/008>.
- [138] B. Wieneke, “Stereo-piv using self-calibration on particle images”, *Experiments in Fluids*, vol. 39, no. 2, pp. 267–280, Aug. 2005, ISSN: 1432-1114. DOI: 10.1007/s00348-005-0962-z. [Online]. Available: <https://doi.org/10.1007/s00348-005-0962-z>.
- [139] Y. Akutina, L. Mydlarski, S. Gaskin, and O. Eiff, “Error analysis of 3d-ptv through unsteady interfaces”, *Experiments in Fluids*, vol. 59, no. 3, p. 53, Feb. 2018, ISSN: 1432-1114. DOI: 10.1007/s00348-018-2509-0. [Online]. Available: <https://doi.org/10.1007/s00348-018-2509-0>.
- [140] H. M. Merklinger, “The ins and outs of focus”, *An Alternative Way To Estimate Depth-of-Field and Sharpness in The Photographic Image, Internet Edition, Published by the author atj http://www.trenholm.org/hmmerk/download.html*, 2002.
- [141] F. Frazier, “Production of artifact casts using epoxy resin”, *Newsletter of Lithic Technology*, pp. 15–21, 1973.
- [142] O. D. Faugeras, Q. .-T. Luong, and S. J. Maybank, “Camera self-calibration: Theory and experiments”, in *Computer Vision — ECCV’92*, G. Sandini, Ed., Berlin, Heidelberg: Springer Berlin Heidelberg, 1992, pp. 321–334, ISBN: 978-3-540-47069-4.
- [143] P. F. Sturm, S. Ramalingam, J.-P. Tardif, S. Gasparini, and J. Barreto, “Camera models and fundamental concepts used in geometric computer vision”, *Foundations and Trends in Computer Graphics and Vision*, vol. 6, pp. 1–183, Jan. 2011.
- [144] C. Steger, “A comprehensive and versatile camera model for cameras with tilt lenses”, *International Journal of Computer Vision*, vol. 123, no. 2, pp. 121–159, Jun. 2017, ISSN: 1573-1405. DOI: 10.1007/s11263-016-0964-8. [Online]. Available: <https://doi.org/10.1007/s11263-016-0964-8>.

- [145] F. Devernay and O. Faugeras, “Straight lines have to be straight”, *Machine Vision and Applications*, vol. 13, no. 1, pp. 14–24, Aug. 2001, ISSN: 1432-1769. DOI: 10.1007/PL00013269. [Online]. Available: <https://doi.org/10.1007/PL00013269>.
- [146] P. Cornic, C. Illoul, A. Cheminet, G. L. Besnerais, F. Champagnat, Y. L. Sant, and B. Leclaire, “Another look at volume self-calibration: Calibration and self-calibration within a pinhole model of scheimpflug cameras”, *Measurement Science and Technology*, vol. 27, no. 9, p. 094004, Aug. 2016. DOI: 10.1088/0957-0233/27/9/094004. [Online]. Available: <https://doi.org/10.1088/0957-0233/27/9/094004>.
- [147] T. Fournel, J.-M. Lavest, S. Coudert, and F. Collange, “Self-calibration of piv video-cameras in scheimpflug condition”, Jan. 2004. DOI: 10.1007/978-3-642-18795-7_28.
- [148] A. Kumar and N. Ahuja, “Generalized radial alignment constraint for camera calibration”, in *2014 22nd International Conference on Pattern Recognition*, Aug. 2014, pp. 184–189. DOI: 10.1109/ICPR.2014.41.
- [149] E. Nocerino, F. Menna, F. Remondino, J.-A. Beraldin, L. Cournoyer, and G. Reain, “Experiments on calibrating tilt-shift lenses for close-range photogrammetry.”, *International Archives of the Photogrammetry, Remote Sensing & Spatial Information Sciences*, vol. 41, 2016.
- [150] B. A. Barsky, D. R. Horn, S. A. Klein, J. A. Pang, and M. Yu, “Camera models and optical systems used in computer graphics: Part i, object-based techniques”, in *Computational Science and Its Applications — ICCSA 2003*, V. Kumar, M. L. Gavrilova, C. J. K. Tan, and P. L’Ecuyer, Eds., Berlin, Heidelberg: Springer Berlin Heidelberg, 2003, pp. 246–255.
- [151] H. Martins, J. Birk, and R. Kelley, “Camera models based on data from two calibration planes”, *Computer Graphics and Image Processing*, vol. 17, no. 2, pp. 173–180, 1981, ISSN: 0146-664X. DOI: [https://doi.org/10.1016/0146-664X\(81\)90024-1](https://doi.org/10.1016/0146-664X(81)90024-1). [Online]. Available: <http://www.sciencedirect.com/science/article/pii/0146664X81900241>.

- [152] S. Ramalingam and P. Sturm, “A unifying model for camera calibration”, *IEEE Transactions on Pattern Analysis and Machine Intelligence*, vol. 39, no. 7, pp. 1309–1319, Jul. 2017, ISSN: 0162-8828. DOI: 10.1109/TPAMI.2016.2592904.
- [153] M. D. Grossberg and S. K. Nayar, “The raxel imaging model and ray-based calibration”, *International Journal of Computer Vision*, vol. 61, no. 2, pp. 119–137, Feb. 2005, ISSN: 1573-1405. DOI: 10.1023/B:VISI.0000043754.56350.10. [Online]. Available: <https://doi.org/10.1023/B:VISI.0000043754.56350.10>.
- [154] C. Sun, H. Liu, M. Jia, and S. Chen, “Review of calibration methods for scheimpflug camera”, *Journal of Sensors*, vol. 2018, 2018.
- [155] N. Otsu, “A threshold selection method from gray-level histograms”, *IEEE Transactions on Systems, Man, and Cybernetics*, vol. 9, no. 1, pp. 62–66, Jan. 1979, ISSN: 0018-9472. DOI: 10.1109/TSMC.1979.4310076.
- [156] A. Trujillo-Pino, K. Krissian, M. Alemán-Flores, and D. Santana-Cedr s, “Accurate subpixel edge location based on partial area effect”, *Image and Vision Computing*, vol. 31, no. 1, pp. 72–90, 2013, ISSN: 0262-8856. DOI: <https://doi.org/10.1016/j.imavis.2012.10.005>. [Online]. Available: <http://www.sciencedirect.com/science/article/pii/S0262885612001850>.
- [157] J. Heikkila, “Geometric camera calibration using circular control points”, *IEEE Transactions on Pattern Analysis and Machine Intelligence*, vol. 22, no. 10, pp. 1066–1077, Oct. 2000, ISSN: 0162-8828. DOI: 10.1109/34.879788.
- [158] J. Mallon and P. F. Whelan, “Which pattern? biasing aspects of planar calibration patterns and detection methods”, *Pattern Recognition Letters*, vol. 28, no. 8, pp. 921–930, 2007, ISSN: 0167-8655. DOI: <https://doi.org/10.1016/j.patrec.2006.12.008>. [Online]. Available: <http://www.sciencedirect.com/science/article/pii/S0167865506003114>.
- [159] A. Hornberg, *Handbook of Machine Vision*. Wiley, 2007, ISBN: 9783527610143. [Online]. Available: <https://books.google.com/books?id=HEy4UBoGF2UC>.

- [160] J. Lavest, G. Rives, and M. Dhome, “Three-dimensional reconstruction by zooming”, *IEEE Transactions on Robotics and Automation*, vol. 9, no. 2, pp. 196–207, Apr. 1993, ISSN: 1042-296X. DOI: 10.1109/70.238283.
- [161] G. P. Stein, “Internal camera calibration using rotation and geometric shapes”, 1993.
- [162] V. L. Orekhov, “A full scale camera calibration technique with automatic model selection–extension and validation”, 2007.
- [163] R. Hartley and S. B. Kang, “Parameter-free radial distortion correction with center of distortion estimation”, *IEEE Transactions on Pattern Analysis and Machine Intelligence*, vol. 29, no. 8, pp. 1309–1321, Aug. 2007, ISSN: 0162-8828. DOI: 10.1109/TPAMI.2007.1147.
- [164] R. Tsai, “A versatile camera calibration technique for high-accuracy 3d machine vision metrology using off-the-shelf tv cameras and lenses”, *IEEE Journal on Robotics and Automation*, vol. 3, no. 4, pp. 323–344, Aug. 1987, ISSN: 0882-4967. DOI: 10.1109/JRA.1987.1087109.
- [165] B. K. Horn, “Tsai’s camera calibration method revisited”, *Online*: http://people.csail.mit.edu/bkph/articles/Tsai_Revisited.pdf, 2000.
- [166] J. H. Brito, R. Angst, K. Köser, and M. Pollefeys, “Radial distortion self-calibration”, in *2013 IEEE Conference on Computer Vision and Pattern Recognition*, Jun. 2013, pp. 1368–1375. DOI: 10.1109/CVPR.2013.180.
- [167] Q. Ji and Y. Zhang, “Camera calibration with genetic algorithms”, *Systems, Man and Cybernetics, Part A: Systems and Humans, IEEE Transactions on*, vol. 31, pp. 120–130, Apr. 2001. DOI: 10.1109/3468.911369.
- [168] K. Ohmi and H.-Y. Li, “Particle-tracking velocimetry with new algorithms”, *Measurement Science and Technology*, vol. 11, no. 6, pp. 603–616, May 2000. DOI: 10.1088/0957-0233/11/6/303. [Online]. Available: <https://doi.org/10.1088/0957-0233/11/6/303>.

- [169] N. T. Ouellette, H. Xu, and E. Bodenschatz, “A quantitative study of three-dimensional lagrangian particle tracking algorithms”, *Experiments in Fluids*, vol. 40, no. 2, pp. 301–313, Feb. 2006, issn: 1432-1114. DOI: 10.1007/s00348-005-0068-7. [Online]. Available: <https://doi.org/10.1007/s00348-005-0068-7>.
- [170] R. Parthasarathy, “Rapid, accurate particle tracking by calculation of radial symmetry centers”, *Nature methods*, vol. 9, pp. 724–6, Jun. 2012. DOI: 10.1038/nmeth.2071.
- [171] A. Rodriguez, H. Zhang, K. Wiklund, T. Brodin, J. Klaminder, P. Andersson, and M. Andersson, “Refining particle positions using circular symmetry”, *PLOS ONE*, vol. 12, no. 4, pp. 1–23, Apr. 2017. DOI: 10.1371/journal.pone.0175015. [Online]. Available: <https://doi.org/10.1371/journal.pone.0175015>.
- [172] S. M. Anthony and S. Granick, “Image analysis with rapid and accurate two-dimensional gaussian fitting”, *Langmuir*, vol. 25, no. 14, pp. 8152–8160, 2009, PMID: 19419178. DOI: 10.1021/la900393v. eprint: <https://doi.org/10.1021/la900393v>. [Online]. Available: <https://doi.org/10.1021/la900393v>.
- [173] P. H. Biwole, W. Yan, Y. Zhang, and J.-J. Roux, “A complete 3d particle tracking algorithm and its applications to the indoor air-flow study”, *Measurement Science and Technology*, vol. 20, no. 11, p. 115 403, Oct. 2009. DOI: 10.1088/0957-0233/20/11/115403. [Online]. Available: <https://doi.org/10.1088/0957-0233/20/11/115403>.
- [174] C. Yi, “Hungarian algorithm for linear assignment problems (v2.3)”, *MATLAB File Exchange*, Retrieved on Oct 2018, Sep 2011. [Online]. Available: <http://csclab.murraystate.edu/bob.pilgrim/445/munkres.html>.
- [175] J. Munkres, “On the assignment and transportation problems (abstract)”, *Naval Research Logistics Quarterly*, vol. 4, no. 1, pp. 77–78, 1957. DOI: 10.1002/nav.3800040112. eprint: <https://onlinelibrary.wiley.com/doi/pdf/10.1002/nav.3800040112>. [Online]. Available: <https://onlinelibrary.wiley.com/doi/abs/10.1002/nav.3800040112>.
- [176] B. K. Horn, *Robot Vision*, 1st. McGraw-Hill Higher Education, 1986, ISBN: 0070303495.

- [177] K. Kraus, *Photogrammetry: geometry from images and laser scans*. Walter de Gruyter, 2011.
- [178] R. I. Hartley and P. Sturm, “Triangulation”, *Comput. Vis. Image Underst.*, vol. 68, no. 2, pp. 146–157, Nov. 1997, ISSN: 1077-3142. DOI: 10.1006/cviu.1997.0547. [Online]. Available: <http://dx.doi.org/10.1006/cviu.1997.0547>.
- [179] K. Kanatani, Y. Sugaya, and H. Niitsuma, “Triangulation from two views revisited: Hartley-sturm vs. optimal correction”, *practice*, vol. 4, p. 5, 2008.
- [180] F. Pereira, H. Stüer, E. C. Graff, and M. Gharib, “Two-frame 3d particle tracking”, *Measurement Science and Technology*, vol. 17, no. 7, pp. 1680–1692, Jun. 2006. DOI: 10.1088/0957-0233/17/7/006. [Online]. Available: <https://doi.org/10.1088/0957-0233/17/7/006>.
- [181] S. J. Baek and S. J. Lee, “A new two-frame particle tracking algorithm using match probability”, *Experiments in Fluids*, vol. 22, no. 1, pp. 23–32, Nov. 1996, ISSN: 1432-1114. DOI: 10.1007/BF01893303. [Online]. Available: <https://doi.org/10.1007/BF01893303>.
- [182] J. Duncan, D. Dabiri, J. Hove, and M. Gharib, “Universal outlier detection for particle image velocimetry (PIV) and particle tracking velocimetry (PTV) data”, *Measurement Science and Technology*, vol. 21, no. 5, p. 057002, Mar. 2010. DOI: 10.1088/0957-0233/21/5/057002. [Online]. Available: <https://doi.org/10.1088/0957-0233/21/5/057002>.
- [183] B. Münch, P. Trtik, F. Marone, and M. Stampanoni, “Stripe and ring artifact removal with combined wavelet — fourier filtering”, *Opt. Express*, vol. 17, no. 10, pp. 8567–8591, May 2009. DOI: 10.1364/OE.17.008567. [Online]. Available: <http://www.opticsexpress.org/abstract.cfm?URI=oe-17-10-8567>.
- [184] V. Pratt, “Direct least-squares fitting of algebraic surfaces”, in *Proceedings of the 14th Annual Conference on Computer Graphics and Interactive Techniques*, ser. SIGGRAPH ’87, New York, NY, USA: ACM, 1987, pp. 145–152, ISBN: 0-89791-227-6. DOI: 10.1145/37401.37420. [Online]. Available: <http://doi.acm.org/10.1145/37401.37420>.

- [185] N. J. Lawson and J. Wu, “Three-dimensional particle image velocimetry: Experimental error analysis of a digital angular stereoscopic system”, *Measurement Science and Technology*, vol. 8, no. 12, pp. 1455–1464, Dec. 1997. DOI: 10.1088/0957-0233/8/12/009. [Online]. Available: <https://doi.org/10.1088/0957-0233/8/12/009>.

Appendices

Appendix A. Correction of perspective and distortion error in calibration data.

Here we are going to explore in more detail the perspective and distortion correction of the calibration data. In Figure 16, we see a circle, say, drawn on a sidewalk seen directly from above (left) and from a pedestrian view (right). Notice, how the circle is transformed into an ellipse when viewed from a side. The center of the circle (orange) is not in the centroid of the ellipse (green). This example demonstrates what happens when we capture calibration targets with two cameras with converging lines of view. Moreover, additional discrepancy is introduced due to various optical distortions present in the camera optics. This phenomenon is a problem because our calibration algorithms rely on centroids of the calibration dots. This leads to a distorted mapping between the physical world and the image reference frames. Let us look closer at the problem. In Figure 17, we see a calibration dot on the left and its image on the right. Image of the circle is transformed into an ellipse due to perspective and distortion effects. We run image processing algorithm to find the center of the ellipse \mathbf{a}_e and empirical calibration to obtain an empirical mapping F_e which maps \mathbf{b}_t to \mathbf{a}_e . Note that ground-truth mapping (F_t) maps \mathbf{b}_t to point \mathbf{a}_t . We call the point which F_t maps onto the center, \mathbf{b}_e . Let us summarize the given below:

$$F_t(\mathbf{b}_e) \equiv \mathbf{a}_e$$

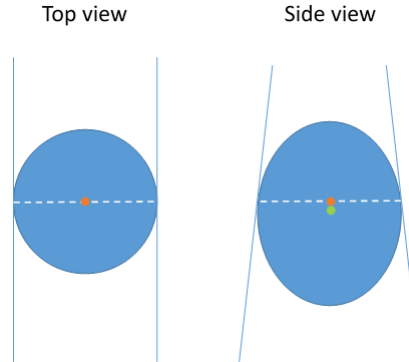


Figure 16: Shift of circle center due to perspective effect.

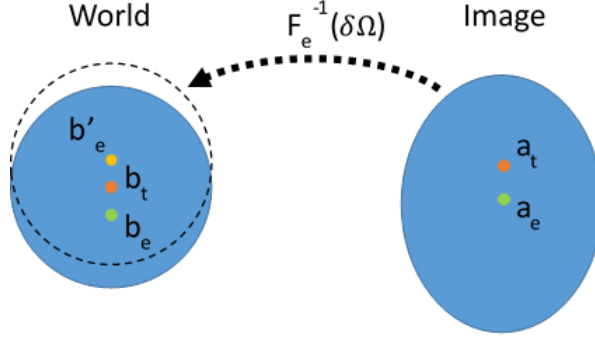


Figure 17: Contour shift due to biased calibration.

$$F_t(\mathbf{b}_t) = \mathbf{a}_t$$

$$F_e(\mathbf{b}_t) = \mathbf{a}_e$$

It follows that:

$$F_e^{-1}(\mathbf{a}_e) - F_t^{-1}(\mathbf{a}_e) = \Delta\mathbf{b}$$

where $\Delta\mathbf{b} = \mathbf{b}_t - \mathbf{b}_e$. We will denote the neighborhood of the dot center in the image space as Ω .

Assumption:

$$F_e^{-1}(\mathbf{x}) - F_t^{-1}(\mathbf{x}) = \Delta\mathbf{b} \quad \forall \mathbf{x} \in \Omega$$

In other words, we assume that in the neighborhood Ω of the image the two inverse mappings differ by a constant shift. This assumption allows us to write that in particular:

$$F_e^{-1}(\boldsymbol{\omega}) - F_t^{-1}(\boldsymbol{\omega}) = \Delta\mathbf{b} \quad \forall \boldsymbol{\omega} \in \delta\Omega \quad (16)$$

where $\delta\Omega$ is the boundary (contour) of the dot image.

We can see how the contours projected by the biased inverse mapping are shifted from the true contours (i.e. ones projected by the true inverse mapping). From the equation 16 we can see that the biased contours are shifted relative to the true contours by vector $\Delta\mathbf{b}$. In this illustration, vector $\Delta\mathbf{b}$ is pointing up. Thus, we get that the center of the biased contours (\mathbf{b}'_e) is a mirror image of \mathbf{b}_e with respect to \mathbf{b}_t . Through this relation, we can find the true mapping since at this point both \mathbf{b}_e and \mathbf{a}_e are known. \mathbf{b}_e can be

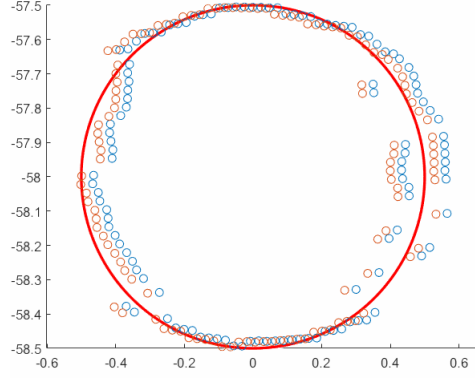


Figure 18: Shift of circle center due to perspective effect. Axes are in mm.

found simply as:

$$\begin{aligned} \mathbf{b}_e &= \mathbf{b}'_e + 2\Delta\mathbf{b} \\ &= -\mathbf{b}'_e + 2\mathbf{b}_t \end{aligned} \tag{17}$$

b_e is found by fitting a circle to the biased inverse projected contours.

Example of this is shown in Figure 18 where the blue dots are the original, biased contours back-projected (F_e^{-1}) onto plane π and the orange ones are the corrected ones. We can see how a circle fitted [184] to the corrected contours is centered around $[0mm, -58mm]$, which is approximately the ground truth for this dot. The summarized algorithm for a single calibration dot then will look like:

1. Find the centroid of the dot image.
2. Perform initial, biased calibration ($F_e(\mathbf{b}_t) = \mathbf{a}_e$).
3. Use the inverse of the biased calibration to map the contours of the dot image into the world ($F_e^{-1}(\delta\Omega)$).
4. Fit a circle to the mapped contour and find its center (b'_e).
5. From \mathbf{b}'_e , find \mathbf{b}_e using equation 17.
6. Use relation $F_t(\mathbf{b}_e) \equiv \mathbf{a}_e$ to find the true mapping.

We can visualize the correction in the form of a vector field where each vector is directed from the biased to corrected center of the dot images as shown in Figure 19. X and Y axes are in pixels. The vectors are scaled. The actual corrections are typically about 0.5px in magnitude.

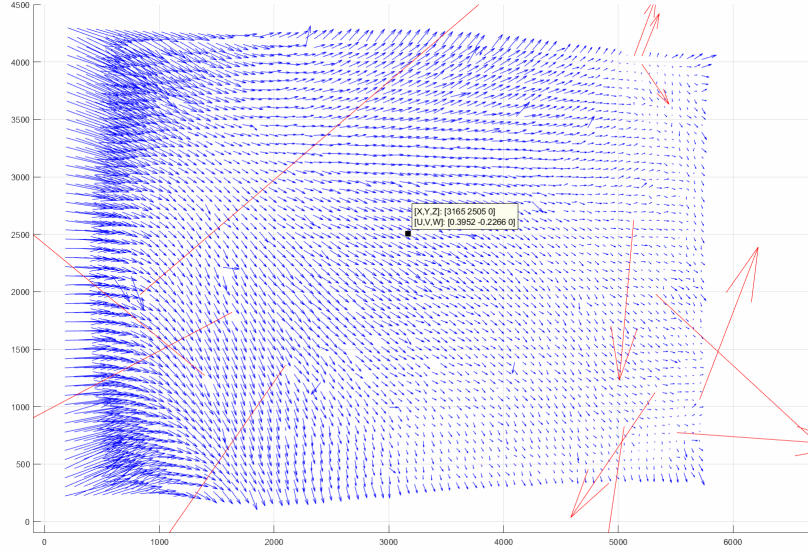


Figure 19: Correction map. Vectors are scaled, typical correction is about $0.5px$. Notice, how vectors are larger on the left, since magnification is larger there. Axes are in pixel units.

Appendix B. Sensitivity analysis.

Based on the values and calibration function obtained experimentally, we ran a few sensitivity studies. We also explore how, given the experimental conditions obtained from calibration, the error in determining particle center in the image affects the triangulation error. The plot showcasing the results of the numerical study is shown in Figure 20. The errors seem to be linearly-dependent with the out-of-plane component of particle position always exceeding its in-plane counterparts. The ratio of the error of the out-of-plane to in-plane components can be controlled by camera tilt [185].

In the table in Figure 21, we can see how uncertainty in the position of the camera projection center (entrance pupil), $p^{(k)}$, affects the uncertainty of triangulation component-by-component. We can see that error in z -position of the particle is moderately sensitive to all x and z components of the position vector of the camera. We also found that the error in y -component of the camera position has negligible effect on the accuracy triangulation. For quantitative information, refer to the plots in Figure 22. Inset in Figure 22 are plots of the reprojection error vs. the error in the camera position. We

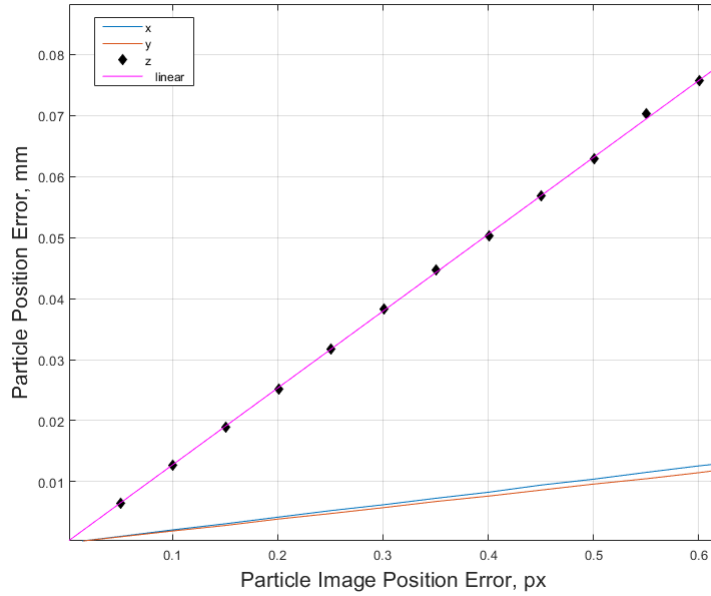


Figure 20: Tabular data for sensitivity of camera position error to particle position error.

find that reprojection error attains minimum at the correct camera position and is convex in the large neighborhood of the minimum. This is promising, as it can potentially be exploited to create a more effective self-calibration routine.

		Particle coordinates		
		x	y	z
Camera coordinates	x	Low	Very low	High
	y	Very low	Low	Low
	z	Low	Very low	Medium

Figure 21: Tabular data for sensitivity of camera position error to particle position error.

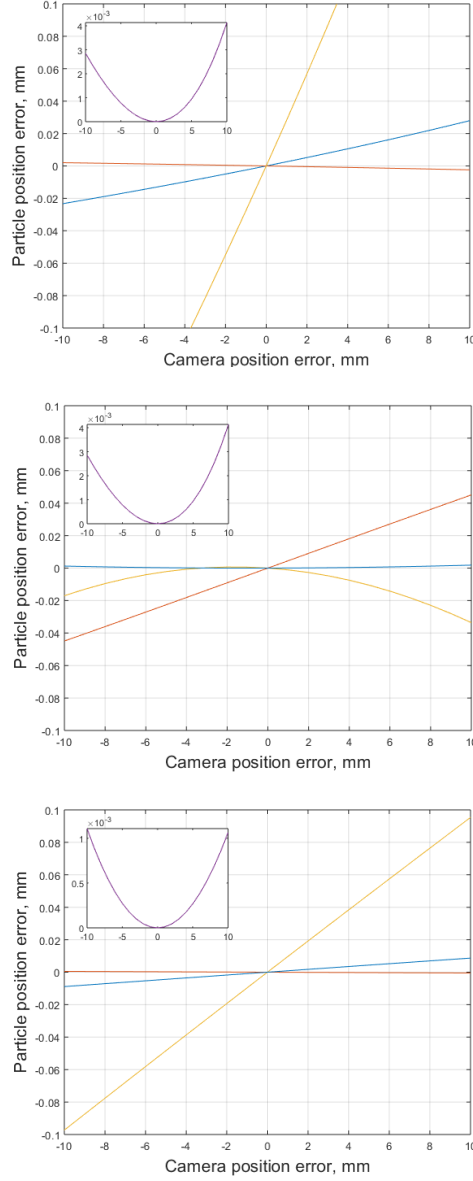


Figure 22: From top to bottom. Sensitivity of particle position error to the error in x (blue), y (red) and z (yellow) position components respectively. Inset are plots of reprojection error vs the error in the respective components.